JEM Journal of Experimental Medicine

ARTICLE

# TET2–STAT3–CXCL5 nexus promotes neutrophil lipid transfer to fuel lung adeno-to-squamous transition

Yun Xue[1,2,3*], Yuting Chen[2,4*], Sijia Sun[5*], Xinyuan Tong[2*], Yujia Chen[5], Shijie Tang[2], Xue Wang[2], Simin Bi[6], Yuqin Qiu[7], Qiqi Zhao[1,2,4], Zhen Qin[2], Qin Xu[2], Yingjie Ai[8], Leilei Chen[5], Beizhen Zhang[3], Zhijie Liu[6], Minbiao Ji[6], Meidong Lang[7,9], Luonan Chen[2,4,10], Guoliang Xu[11,12], Liang Hu[2], Dan Ye[5], and Hongbin Ji[1,2,4]

**Phenotypic plasticity is a rising cancer hallmark, and lung adeno-to-squamous transition (AST) triggered by LKB1 inactivation is significantly associated with drug resistance. Mechanistic insights into AST are urgently needed to identify therapeutic vulnerability in LKB1-deficient lung cancer. Here, we find that ten-eleven translocation (TET)–mediated DNA demethylation is elevated during AST in *Kras*$^{LSL\text{-}G12D/+}$; *Lkb1*$^{L/L}$ (*KL*) mice, and knockout of individual *Tet* genes reveals that *Tet2* is required for squamous transition. TET2 promotes neutrophil infiltration through STAT3-mediated CXCL5 expression. Targeting the STAT3–CXCL5 nexus effectively inhibits squamous transition through reducing neutrophil infiltration. Interestingly, tumor-infiltrating neutrophils are laden with triglycerides and can transfer the lipid to tumor cells to promote cell proliferation and squamous transition. Pharmacological inhibition of macropinocytosis dramatically inhibits neutrophil-to–cancer cell lipid transfer and blocks squamous transition. These data uncover an epigenetic mechanism orchestrating phenotypic plasticity through regulating immune microenvironment and metabolic communication, and identify therapeutic strategies to inhibit AST.**

## Introduction

Phenotypic plasticity is a rising hallmark of cancer (Hanahan, 2022). For instance, adeno-to-squamous transition (AST) in lung cancer represents a typical histological transformation associated with strong cancer plasticity, the capability to switch between different lineages (Hou et al., 2016; Kanazawa et al., 2000; Qin et al., 2024). Clinical data show that squamous transition occurs in certain patients with lung adenocarcinoma (ADC) who relapse after molecularly targeted therapy using tyrosine-kinase inhibitors or KRAS inhibitor (Lin et al., 2020; Schoenfeld et al., 2020; Awad et al., 2021). Somatic loss-of-function mutations of *LKB1* (also named serine-threonine kinase 11, *STK11*) are frequently observed in lung cancer and associated with strong cancer plasticity (Ji et al., 2007; Koivunen et al., 2008; Li et al., 2015; Tong et al., 2024). *LKB1* is mutated in ∼17% of human ADC (Quintanal-Villalonga et al., 2021a). In contrast, human lung adenosquamous cell carcinoma (AdSCC), which features mixed pathologies containing both adenomatous and squamous lesions within single tumors and is associated with worse patient survival, displays an enrichment of *LKB1* mutations at 39.7%, ranging from 22% to 66% according to multiple studies (Matsumoto et al., 2007; Koivunen et al., 2008; Zhang et al., 2017; Krause et al., 2020; Quintanal-Villalonga et al., 2021a;

[1]Key Laboratory of Systems Health Science of Zhejiang Province, School of Life Science, Hangzhou Institute for Advanced Study, University of Chinese Academy of Sciences, Hangzhou, China; [2]Key Laboratory of Multi-Cell Systems, Shanghai Institute of Biochemistry and Cell Biology, Center for Excellence in Molecular Cell Science, Chinese Academy of Sciences, Shanghai, China; [3]University of Chinese Academy of Sciences, Beijing, China; [4]School of Life Science and Technology, Shanghai Tech University, Shanghai, China; [5]Shanghai Key Laboratory of Medical Epigenetics, International Co-laboratory of Medical Epigenetics and Metabolism (Ministry of Science and Technology), and Molecular and Cell Biology Laboratory, Institutes of Biomedical Sciences, Shanghai Medical College of Fudan University, Shanghai, China; [6]Department of Physics, State Key Laboratory of Surface Physics, Academy for Engineering and Technology, Key Laboratory of Micro and Nano Photonic Structures (Ministry of Education), Shanghai, China; [7]Key Laboratory of Advanced Polymeric Materials, School of Materials Science and Engineering, East China University of Science and Technology, Shanghai, China; [8]Department of Gastroenterology and Hepatology, Zhongshan Hospital, Fudan University, Shanghai, China; [9]Department of General Surgery and Laboratory of General Surgery, Xinhua Hospital, Affiliated to School of Medicine, Shanghai Jiao Tong University, Shanghai, China; [10]Center for Excellence in Animal Evolution and Genetics, Chinese Academy of Sciences, Kunming, China; [11]State Key Laboratory of Molecular Biology, Shanghai Institute of Biochemistry and Cell Biology, Center for Excellence in Molecular Cell Science, Chinese Academy of Sciences, University of Chinese Academy of Sciences, Shanghai, China; [12]Shanghai Key Laboratory of Medical Epigenetics, Institutes of Biomedical Sciences, Shanghai Medical College of Fudan University, Chinese Academy of Medical Sciences (RU069), Shanghai, China.

*Y. Xue, Yuting Chen, S. Sun, and X. Tong contributed equally to this paper. Correspondence to Hongbin Ji: hbji@sibcb.ac.cn; Dan Ye: yedan@fudan.edu.cn; Liang Hu: liang.hu@sibcb.ac.cn

H. Ji is the lead contact.

Tang et al., 2023). Quintanal-Villalonga et al. (2021a) have recently analyzed *LKB1* mutations in lung tumors with squamous transition after drug resistance acquisition. This study shows an occurrence rate of *STK11/LKB1* mutations at 14.3% (one out of seven) in relapsed patients with potential AST, largely due to their mutual exclusivity with epidermal growth factor receptor (*EGFR*) mutations (Sanchez-Cespedes et al., 2002; Mahoney et al., 2009; Ab Mutalib et al., 2014; Quintanal-Villalonga et al., 2021a). When samples with *EGFR* mutations were excluded from this dataset, the *STK11/LKB1* mutation was observed in one out of three samples (33%) (Quintanal-Villalonga et al., 2021a). Previous studies show a prevalence of *LKB1* mutations at about 39.7% in human lung AdSCC, similar to that observed in relapsed patients with potential AST (Matsumoto et al., 2007; Koivunen et al., 2008; Zhang et al., 2017; Krause et al., 2020; Quintanal-Villalonga et al., 2021a; Tang et al., 2023).

Consistent with these clinical observations, *LKB1* deficiency has been proven to be able to drive transition from ADC to squamous cell carcinoma in a $Kras^{LSL\text{-}G12D/+}$; $Lkb1^{L/L}$ (*KL*) mouse model (Han et al., 2014; Gao et al., 2014; Li et al., 2015; Zhang et al., 2017). We have previously shown that a decreased lysyl oxidase level and consequent extracellular matrix (ECM) remodeling serve as the important trigger for AST in the *KL* model as well as in $Kras^{LSL\text{-}G12D/+}$; $Trp53^{L/L}$ mouse model, a classical ADC model (Han et al., 2014; Yao et al., 2018, *Preprint*). Moreover, we find that yes-associated protein (*YAP*) inactivation resulting from ECM remodeling precedes the appearance of squamous biomarker p63 and histological transformation in the *KL* model (Gao et al., 2014). The ECM remodeling seems associated with uncontrolled accumulation of excessive oxidative stress, which accelerates the process of AST (Li et al., 2015). We also find that histone methyltransferase EZH2 inhibits squamous transition by altering the expression of squamous differentiation-related genes (Zhang et al., 2017). Despite all these efforts, the epigenetic regulatory mechanisms in AST, especially associated with DNA methylation status, still remain elusive.

DNA methylation is reversibly and delicately regulated by multiple enzymes including DNA methyltransferases (DNMTs) and ten-eleven translocation (TET) family of DNA hydroxylases (Yin et al., 2017; Wu and Zhang, 2014). The TET family of proteins are composed of TET1, TET2, and TET3, which catalyze serial oxidation reactions: converting 5-methylcytosine (5mC) to 5-hydroxymethylcytosine (5hmC), then to 5-formylcytosine, and eventually to 5-carboxylcytosine (Tahiliani et al., 2009; Ito et al., 2011; He et al., 2011). Extensive studies have highlighted the tumor-suppressive role of TET family proteins in leukemia. Our recent work using a genetically engineered mouse model (GEMM) also identifies TET2 as a tumor suppressor in *Kras*-driven ADC (Xu et al., 2022). However, whether TET enzymes participate in AST is unclear.

Increased neutrophil infiltration is frequently observed during the AST process and is associated with squamous pathology (Xu et al., 2014; Koyama et al., 2016). Previous studies also show that temporary depletion of neutrophils could dampen squamous transition (Koyama et al., 2016; Mollaoglu et al., 2018). However, it remains unclear how neutrophil accelerates the AST process. Tumor-infiltrating neutrophils are known to promote angiogenesis and immunosuppression in the tumor microenvironment by releasing proinflammatory factors (Dumitru et al., 2013). A recent study also shows that neutrophil extracellular traps might help attract cancer cells to form distant metastases (Yang et al., 2020). A later study finds that lung neutrophils are laden with lipids and create a premetastatic niche for breast cancer (Li et al., 2020a). It remains interesting to investigate how lung neutrophil contributes to AST.

With the integrative analyses of GEMMs and clinical specimens, we here identify TET2 as an important epigenetic regulator of AST. Our results also link the TET2-mediated epigenetic mechanism to neutrophil infiltration and neutrophil–cancer cell lipid transfer during the AST process and identify multiple therapeutic strategies to inhibit lung AST.

## Results

### *Tet2* knockout (KO) inhibits lung adeno-to-squamous transition

To study the potential link between DNA methylation and AST, we first analyzed the expression of DNA methylation regulators in normal lungs, ADC, and squamous cell carcinoma (SCC) from the *KL* model (Fig. 1 A). We found that KL-SCC exhibited the upregulation of *Dnmt1*, *Dnmt3a*, and *Uhrf1* when compared with KL-ADC. Upregulation of *Tet2* and *Tet3*, but not *Tet1*, was also observed in KL-SCC (Fig. 1 A). Using the TCGA-NSCLC datasets, we found that human lung squamous cell carcinoma (LUSC) exhibited upregulation of *DNMT* and *TET* gene expression compared with human lung adenocarcinoma (LUAD) (Fig. S1 A), indicative of a potential link of *DNMT* or *TET* with lung cancer pathologies. We focused on the roles of TETs in this process. In agreement with the upregulation of *TET* expression, immunohistochemistry (IHC) staining demonstrated that the levels of 5mC and 5hmC were higher in KL-SCC than KL-ADC (Fig. S1, B–D), further implying a potential role of TET and DNA demethylation in lung AST.

We then performed CRISPR/Cas9-mediated *Tet* (*Tet1/2/3*) gene KO in the *KL* model through lentivirus nasal inhalation as previously described (Sánchez-Rivera et al., 2014; Wu et al., 2018). DNA sequencing confirmed the proper edits in the targeted alleles (Fig. S1 E). We further confirmed the KO efficiency of *Tet2* by western blot analysis (Fig. S1 F). We observed a remarkable decrease in global 5hmC levels in *Tet2* KO tumors, but not *Tet1* KO or *Tet3* KO tumors (Fig. S1 G). Interestingly, only *Tet2* KO dramatically suppressed squamous transition (Fig. S1 H), as evidenced by the fact that most tumors showed ADC pathology with high TTF1 expression and no p63, SOX2, and KRT5 expression (Fig. S1 I). *Tet2* KO also reduced the AST incidence, the number, and burden of SCC in the *KL* model (Fig. S1, J–L). In agreement with the transcriptome data (Fig. 1 A), western blot data further confirmed the upregulation of TET2 protein in KL-SCC (Fig. 1 B). These results indicate that *Tet2*, but not *Tet1* or *Tet3*, may be important for AST in the *KL* model.

We next generated a conditional $Kras^{LSL\text{-}G12D/+}$; $Lkb1^{L/L}$; $Tet2^{L/L}$ (*KLT*) mouse strain for AST analyses (Fig. 1 C). *Tet2* KO efficiency was confirmed by western blot analysis (Fig. S2 A). Further PCR analysis verified *Tet2* KO in cancer cells ($CD45^-/EpCAM^+$) but

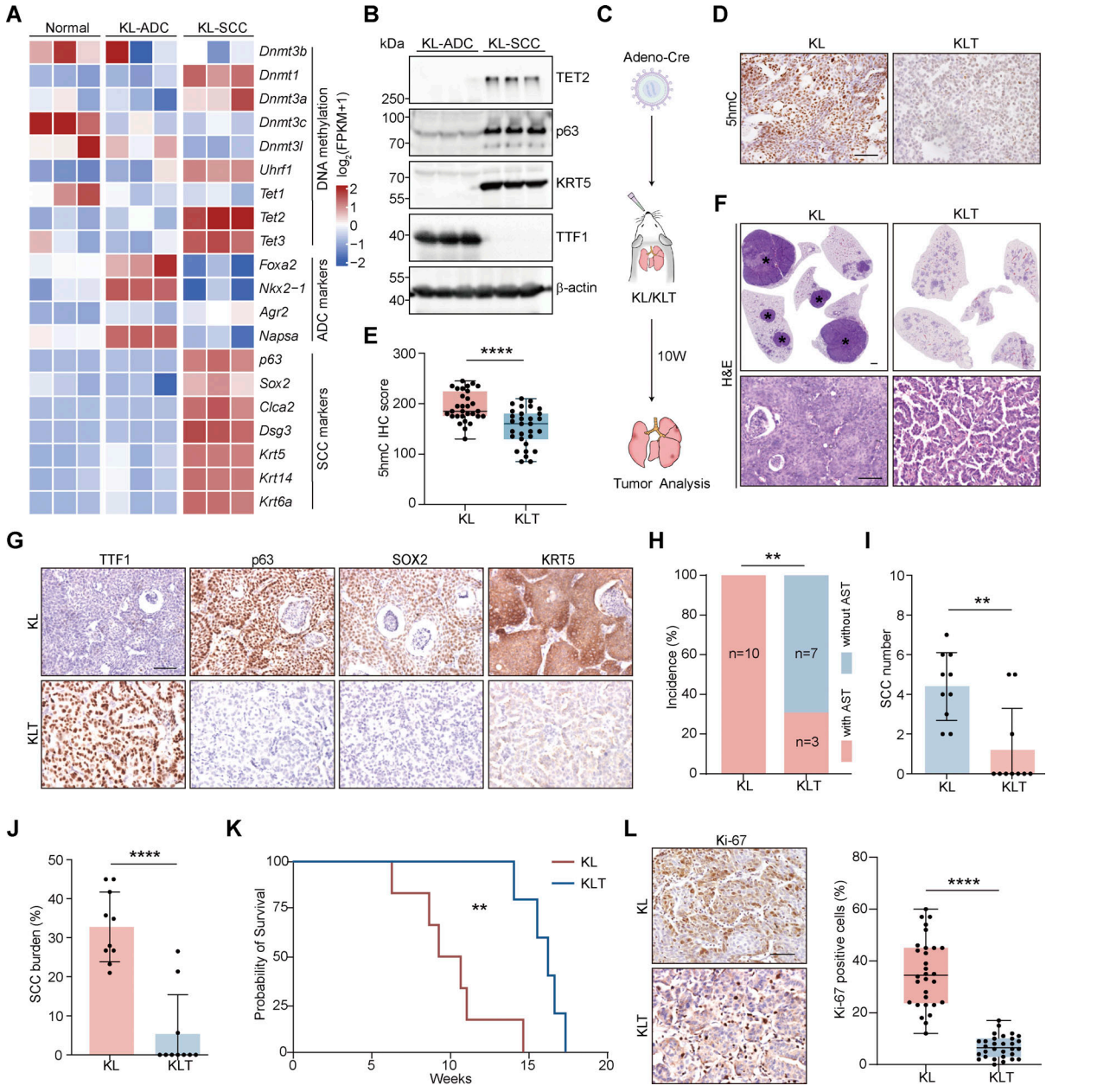


Figure 1. ***Tet2* KO inhibits squamous transition in *KL* model. (A)** Heatmap of DNA methylation factors and adeno/squamous lineage markers in normal lung, ADC, and SCC of the *KL* mouse model. **(B)** Western blot analysis for TET2, p63, KRT5, and TTF1 in KL-ADC and KL-SCC tumors. β-Actin served as the internal loading control. Parallel blots using the same samples. **(C)** Schematic illustration of the *KL* and *KLT* mouse model. W, week. **(D and E)** (D) Representative 5hmC IHC staining of *KL* and *KLT* tumors. Scale bar: 50 µm. Statistical analysis is also shown (E). 30 representative images for each group were counted. **(F)** Representative H&E staining for whole lungs of *KL* and *KLT* models. The whole lungs are reused in Fig. S2 E. * indicates SCC. Scale bar: 1 mm. H&E staining with high magnification is shown. Scale bar: 50 µm. **(G)** Representative IHC staining for TTF1, p63, SOX2, and KRT5 in *KL* and *KLT* mice. Scale bar: 50 µm. **(H–J)** Statistical analyses of the AST incidence (H), the number (I), and burden (J) of SCC in *KL* ($n$ = 10) and *KLT* ($n$ = 10) mice. **(K)** Kaplan–Meier survival curves of *KL* ($n$ = 6) and *KLT* ($n$ = 5) mice. **(L)** Representative Ki-67 IHC staining and statistical analyses in *KL* and *KLT* tumors. Scale bar: 50 µm. 30 representative images for each group were counted. Data in B, D, and E represent one experiment of three independent repeats, and F–L represents one experiment of two independent repeats. **P < 0.01, ****P < 0.0001 by two-tailed unpaired Student's $t$ test (E, I, J, and L), Fisher's exact test (H), log-rank (Mantel–Cox) test (K). Data are represented as mean ± SD. Source data are available for this figure: SourceData F1.

not in immune cells (CD45$^+$/EpCAM$^-$) isolated from *KLT* lung tumors (Fig. S2 B). In agreement with our earlier finding (Fig. S1 G), *Tet2* KO resulted in a dramatic reduction of 5hmC level (Fig. 1, D and E). We found that *Tet2* KO increased the growth of ADC (Fig. S2, C and D), consistent with our previous study about the suppressive role of *Tet2* in *Kras*$^{G12D}$-driven ADC (Xu et al., 2022). Interestingly, *Tet2* KO dramatically suppressed squamous transition (Fig. 1, F and G; and Fig. S2 E). Statistical analyses also showed a significant decrease of AST incidence, the number, and burden of SCC in *KLT* mice (Fig. 1, H–J). Moreover, the *KLT* mouse survival was prolonged compared with *KL* mice (Fig. 1 K). IHC staining of Ki-67 confirmed a remarkable decrease in cell

proliferation in *KLT* total lung tumors (Fig. 1 L). These data together identify TET2 as an important regulator of AST in the *KL* model.

### *Tet2* KO inhibits neutrophil infiltration into *KL* tumor microenvironment

We further checked if TET2 regulated the gene expression of squamous lineage markers. We found that *Tet2* KO in *KL* squamous organoids didn't affect the expression of *p63*, *Sox2*, *Krt5*, and *Krt14* (Fig. S2, F and G). Moreover, ectopic expression of wild-type *TET2* or its catalytically inactive mutant (Xu et al., 2022) failed to alter the expression of squamous markers (Fig. S2, H and I). These results indicate that *Tet2* might not directly regulate squamous transition.

Tumor immune microenvironment is frequently observed with an alteration during lung AST, e.g., fewer T lymphocytes with higher expression of immune checkpoint receptor and increased numbers of neutrophils were detected in *KL* model when compared with $Kras^{LSL-G12D/+}$; $Trp53^{L/L}$(*KP*) model, a typical ADC mouse model (Koyama et al., 2016). Through transcriptomic analyses of KL-ADC and KL-SCC using gene set variation analysis (GSVA), we found that inflammatory signaling pathways, especially the interferon (IFN) pathway, were significantly enriched in KL-SCC (Fig. S3 A). Consistently, immunofluorescence (IF) staining for myeloperoxidase (MPO) showed that neutrophil infiltration was remarkably increased in KL-SCC (Fig. S3, B and C).

To test the early change of tumor immune microenvironment, we performed flow cytometry analysis of the dissociated lung tumor from *KL* and *KLT* mice at 7 wk after Adeno-Cre infection, a time point when all tumors uniformly maintained ADC pathology (Fig. S3, D–G) (Han et al., 2014). Despite comparable tumor burdens (Fig. S3, D and E), we observed a dramatic decrease of neutrophils ($CD11b^+/Ly6G^+/CD45^+$) in *KLT* tumors (Fig. 2 A and Fig. S3 H), which was further confirmed by MPO staining (Fig. 2, B and C). We compared neutrophil infiltration between the 7- and 9-wk tumors from the *KLT* model and found no significant change over this period (Fig. S3 I). Besides neutrophils, tumor-associated macrophages (TAM) were found to be elevated in *KLT* tumors, with dominant M1-like TAM ($F4/80^+/CD11c^{low(lo)}/CD11b^{high(hi)}/CD45^+$) (Fig. 2 A and Fig. S3 H). No substantial change of $CD4^+$ T cells ($CD4^+/CD3^+/CD45^+$), $CD8^+$ T cells ($CD8^+/CD3^+/CD45^+$), regulatory T (Treg) cells ($Foxp3^+/CD4^+/CD3^+/CD45^+$), natural killer cells (NK, $CD49b^+/CD3^-/CD45^+$), or natural killer T cells (NKT, $CD49b^+/CD3^+/CD45^+$) was observed (Fig. 2 A and Fig. S3 H).

### TET2 enhances neutrophil infiltration through CXCL5 production

Increased neutrophil infiltration is established as a typical inflammatory feature associated with AST, and depletion of neutrophils dampens squamous transition (Koyama et al., 2016; Mollaoglu et al., 2018). We then investigated how TET2 promotes neutrophil infiltration during AST. It is known that *KL* tumor cells can stimulate neutrophil recruitment through the production of cytokines and chemokines (Koyama et al., 2016). An appealing hypothesis is that TET2 in *KL* tumor cells might regulate the expression of genes involved in the neutrophil chemotaxis pathway. The CXCL subfamily (e.g., CXCL1, CXCL2, CXCL3, and CXCL5) preferentially attracts neutrophils to the inflamed site (Zlotnik and Yoshie, 2000; Palomino and Marti, 2015). We found that *Cxcl3* and *Cxcl5* were greatly upregulated in KL-SCC compared with KL-ADC whereas *Tet2* KO only led to downregulation of *Cxcl5* gene transcription in *KLT* tumors (Fig. S3, J and K). These findings indicate that *Cxcl5* but not *Cxcl3* may be one of the downstream targets of TET2, which contributes to neutrophil recruitment to tumor microenvironment.

We further confirmed the downregulation of CXCL5 protein in *KLT* tumors by ELISA (Fig. 2 D). Using CXCL5-neutralizing antibody treatment, we found that αCXCL5 decreased CXCL5 expression and neutrophil infiltration, as indicated by less MPO-positive staining in *KL* lung tumors (Fig. 2, E–G). Moreover, αCXCL5 treatment suppressed squamous transition (Fig. 2 H and Fig. S3 L). The αCXCL5 treatment showed a tendency to downregulate the AST incidence and significantly decreased the number and burden of SCC (Fig. 2, I–K). We also observed a dramatic decrease in cell proliferation in all lung tumors from the αCXCL5 treatment group (Fig. 2 L).

To further ascertain the role of CXCL5 in AST, we performed *Cxcl5* KO using the CRISPR-Cas9 system in the *KL* model. We found that CXCL5 level and neutrophil infiltration were remarkably decreased in the sg*Cxcl5* group (Fig. 2 M and Fig. S3 M). Consistently, *Cxcl5* KO dramatically suppressed squamous transition, as evidenced by the fact that most tumors showed ADC pathology with high TTF1 expression and no p63, SOX2, and KRT5 expression (Fig. 2 N; and Fig. S3, N and Q). As a result, *Cxcl5* KO reduced the AST incidence, and the number and burden of SCC (Fig. 2 O; and Fig. S3, O and P). These data together with αCXCL5 treatment results support an important role of CXCL5 in TET2-mediated neutrophil infiltration and AST.

### The TET2–STAT3–CXCL5 nexus enhances neutrophil infiltration

To elucidate how TET2 regulates CXCL5, we established two independent primary tumor cell lines derived from *KL* tumors (hereafter referred to as KL-#1 and KL-#2 cells). We found that *Tet2* KO didn't have a major effect on *Cxcl5* expression in both cell lines (Fig. 3, A and B; and Fig. S4, A and B), in contrast to the dramatic downregulation of *Cxcl5* in *KLT* tumors (Fig. S3 K). We noticed that the IFN pathway was enriched in KL-SCC (Fig. S3 A), indicating that the inflammatory signals may be important for the AST process. Notably, upon mouse IFNγ (mIFNγ) stimulation, *Tet2* KO significantly downregulated *Cxcl5* transcriptional expression in both cell lines (Fig. 3, A and B; and Fig. S4, A and B). Using hydroxymethylated DNA immunoprecipitation (hMeDIP) quantitative PCR (qPCR) assay, we found that mIFNγ treatment remarkably increased the 5hmC level at *Cxcl5* proximal promoter region (−1,099 ∼ −855 bp) of the transcription start site (TSS), and such increase was completely abolished by *Tet2* KO (Fig. 3, C–E). These data indicated the involvement of TET2 in *Cxcl5* promoter regulation. Using chromatin immunoprecipitation (ChIP)-qPCR assay, we further found that mIFNγ treatment promoted the binding of TET2 to *Cxcl5* promoter (Fig. 3 F). TET2 is known to be recruited to DNA by multiple

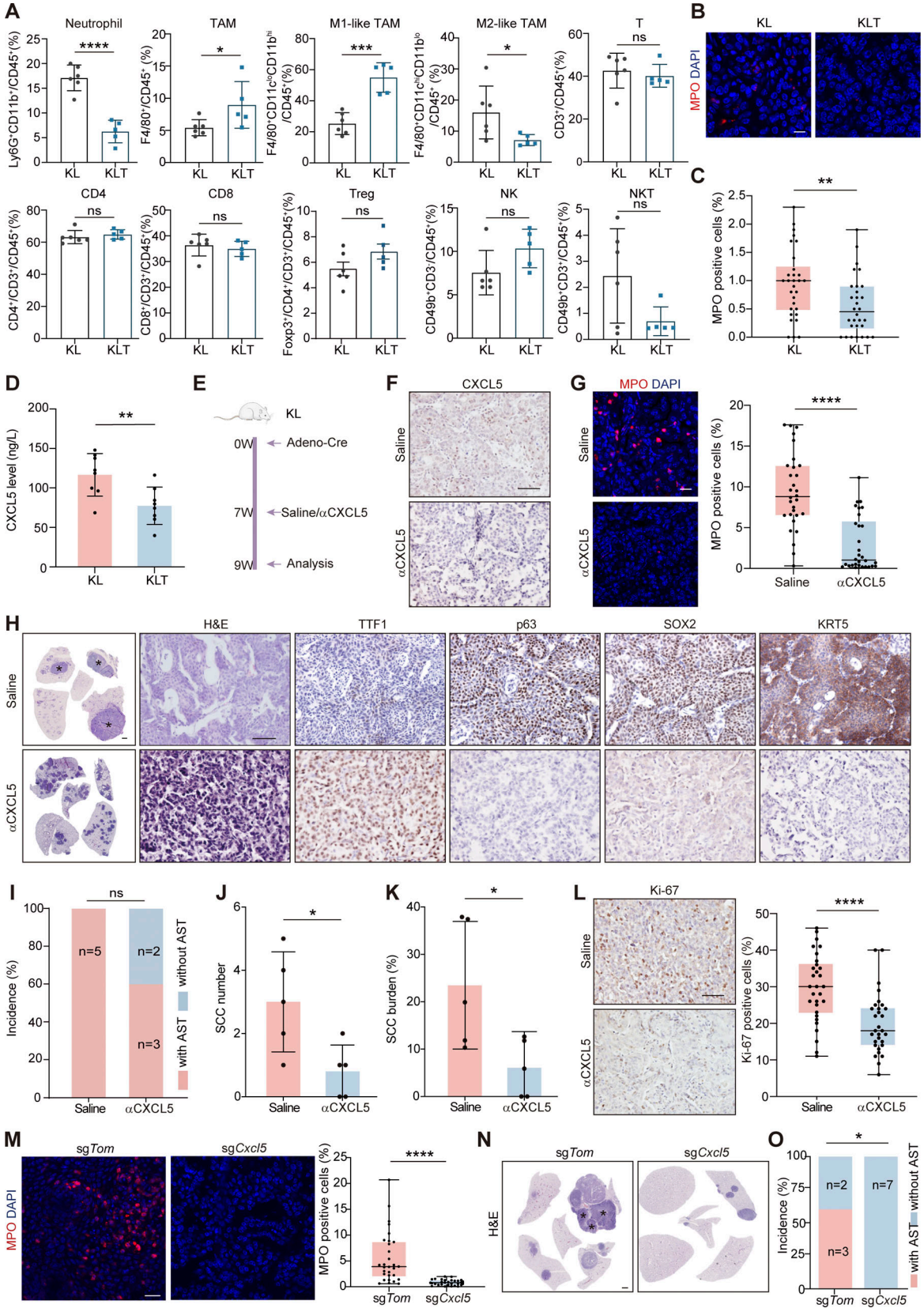


Figure 2. **TET2 promotes neutrophil infiltration and AST potentially through CXCL5 production. (A)** The percentage of indicated immune subpopulations in *KL* ($n$ = 6) and *KLT* ($n$ = 5) mouse lungs. Each dot represents one mouse. **(B and C)** (B) Representative fluorescence staining of neutrophil (MPO-positive cells) infiltration in *KL* and *KLT* tumors; red: MPO; blue: DAPI. Scale bar: 20 µm. Statistical analyses (C). 30 representative images for each group were counted. **(D)** ELISA assay detection of CXCL5 protein levels in *KL* ($n$ = 8) and *KLT* ($n$ = 8) lung tumors. **(E)** Schematic illustration of αCXCL5 treatment

experiment. W, week. **(F)** Representative CXCL5 IHC staining in *KL* lung tumors. Scale bar: 50 µm. **(G)** Representative fluorescence staining of neutrophil (MPO-positive cells) infiltration in *KL* mice treated with saline and αCXCL5. red: MPO; blue: DAPI. Scale bar: 20 µm. Statistical analysis is shown on the right. The statistical fields include both ADC and SCC pathologies. 30 representative images for each group were counted. **(H)** Representative H&E staining and IHC staining in *KL* mice treated with saline or αCXCL5. The whole lungs are reused in Fig. S3 L. * indicates SCC. Scale bar for whole lung: 1 mm; scale bar for others: 50 µm. **(I–K)** Statistical analyses of the AST incidence (I), the number (J), and burden (K) of SCC in *KL* mice treated with saline ($n$ = 5) or αCXCL5 ($n$ = 5). **(L)** Representative Ki-67 IHC staining and statistical analyses in *KL* mice treated with saline or αCXCL5. Scale bar: 50 µm. 30 representative images for each group were counted. **(M)** Representative fluorescence staining of neutrophils (MPO-positive cells) in *KL* tumors with sg*Tom* or sg*Cxcl5*. red: MPO; blue: DAPI. Scale bar: 20 µm. Statistical analyses are shown on the right. The statistical fields include both ADC and SCC pathologies. 30 representative images for each group were counted. **(N)** Representative whole lungs of *KL* model with sg*Tom* or sg*Cxcl5*. The whole lungs are reused in Fig. S3 Q. * indicates SCC. Scale bar: 1 mm. **(O)** Statistical analyses of the AST incidence in *KL* model with sg*Tom* ($n$ = 5) or sg*Cxcl5* ($n$ = 7). Data in A–D represent one experiment of three independent repeats, and F–O represent one experiment of two independent repeats. *P < 0.05, **P < 0.01, ***P < 0.001, ****P < 0.0001 by two-tailed unpaired Student's $t$ test (A, C, D, G, and J–M), Fisher's exact test (I and O). ns: not significant. Data are represented as mean ± SD.

sequence-specific transcription factors (Català-Moll et al., 2022; Wu and Zhang, 2014). Of note, the *Cxcl5* proximal promoter region contained a putative binding motif for STAT3 around, −1,300 bp, near TSS (Fig. 3 G). We found that both total STAT3 and its active form (phosphorylated-STAT3, pSTAT3) were upregulated by mIFNγ treatment (Fig. S4 C). IP data further confirmed the interaction between TET2 and STAT3 (Fig. 3 H). We also found that the binding of TET2 to *Cxcl5* promoter was abrogated by *Stat3* KO (Fig. 3 I; and Fig. S4, D and E). Along with reduced TET2 occupancy at *Cxcl5* promoter, *Stat3* KO led to decreased 5hmC enrichment (Fig. 3 J) at *Cxcl5* promoter and *Cxcl5* expression (Fig. 3, K and L).

Ruxolitinib (Ruxo) is a clinically approved specific inhibitor of JAK1/2 that inhibits the JAK-STAT signaling (Lussana et al., 2018; Ajayi et al., 2018; Modi et al., 2019). We found that Ruxo treatment suppressed the effects of mIFNγ on STAT3 phosphorylation (Fig. S4, F and G), 5hmC enrichment at *Cxcl5* promoter (Fig. 3 J), and *Cxcl5* gene expression (Fig. 3, K and L). C188-9 (also named TTI-101) is a potent small molecule specifically targeting the Src-homology 2 domain of STAT3 currently under clinical development (Jung et al., 2017; Johnson et al., 2018; Pan et al., 2022). We found that C188-9 treatment also significantly inhibited the effects of mIFNγ on STAT3 phosphorylation (Fig. S4, F and G) and *Cxcl5* gene expression (Fig. 3 L). We then treated the *KL* mouse model with Ruxo or C188-9 for 2 wk (Fig. 4 A and Fig. S4 H). We found that either inhibitor administration led to reduced levels of pSTAT3 and CXCL5 and suppressed neutrophil infiltration in the *KL* model (Fig. 4, B and C; and Fig. S4, I and J). Importantly, Ruxo or C188-9 treatment could inhibit the AST process in the *KL* model, as evidenced by the fact that most tumors showed ADC pathology with high TTF1 expression and no p63, SOX2, and KRT5 expression (Fig. 4, D and I; and Fig. S4, K and L). As a result, the incidence of AST exhibited a tendency to decrease, whereas the number and burden of SCC, as well as cell proliferation, were significantly reduced in the inhibitor-treated groups (Fig. 4, E–H, and J–M). These data together reaffirm the functional importance of TET2–STAT3–CXCL5 nexus in facilitating neutrophil infiltration and AST in the *KL* model.

### Lipid-laden neutrophils fuel the AST process

A recent study shows that lung neutrophils are laden with lipids and able to transfer lipid to breast cancer cells to facilitate metastasis (Li et al., 2020a). Through Boron dipyrromethene (BODIPY) IF staining analyses, we found that the KL-SCC showed the highest level of lipid than KL-ADC and KLT-ADC. Moreover, KLT-ADC showed very low BODIPY staining (Fig. S5 A). These data indicated a potential link between lipid dysregulation and *TET2* KO as well as AST. We next performed flow cytometry analysis to test what types of cells were laden with lipid. Indeed, we found that lipid levels were significantly increased in both neutrophils and tumor cells from KL-SCC when compared with KL-ADC or KLT-ADC (Fig. 5 A and Fig. S5 B). This was further confirmed by IF staining (Fig. 5 B and Fig. S5 C). Through applying the imaging technique of stimulated Raman scattering (SRS) microscopy, we found that KL-SCC exhibited the highest level of lipid when compared with KL-ADC and KLT-ADC (Fig. 5 C and Fig. S5, D–F). Using SRS microscopy analysis and standard samples, we were able to distinguish triacylglycerol (TG), cholesterol and phospholipids mainly containing phosphatidylcholine (PC), phosphatidylethanolamine (PE), phosphatidylserine (PS), and sphingomyelin (SM) (Vance, 2015) (Fig. S5 G). We found that TG, but not cholesterol or phospholipids, was the major component of increased lipid in KL-SCC (Fig. S5 H). Loss of *Tet2* mainly decreased the TG level in KLT tumors, as evidenced by SRS microscopy (Fig. 5 C) and BODIPY staining analyses (Fig. S5 A).

Considering the highly lipid-laden phenotype of neutrophils, we hypothesized that lipid transfer from neutrophils to cancer cells might promote tumor growth. Macropinocytosis is known to assist tumor cells in ingesting neutrophil-derived TG (Li et al., 2020a). When cocultured with neutrophils isolated from KL-SCC, we observed a dramatic increase in lipid accumulation in KL cells (Fig. 5, D and E). Treatment with 5-(N-ethyl-N-isopropyl) amiloride (EIPA), which inhibits macropinocytosis (Kim et al., 2018), completely blocked the lipid acquisition of KL cells (Fig. 5, D and E). Costaining of BODIPY and Ki-67 further demonstrated that the proliferation of KL cells was increased when cocultured with KL-SCC–derived neutrophils (Fig. 5, F–H; and Fig. S5, I–K). Such an increase was profoundly blocked by EIPA treatment (Fig. 5, F–H; and Fig. S5, I–K). We further determined the effect of TG supplementation on KL cell growth. To this end, we encapsulated TG within micelles as previously described (Dai et al., 2017; Goncalves et al., 2015). Interestingly, we found that the treatment with TG-micelles dramatically promoted lipid accumulation and increased cell proliferation in KL cells, which could be diminished by EIPA treatment (Fig. 5, I–K; and Fig. S5 L). These data support the role of TG transfer in promoting KL-SCC cell proliferation.

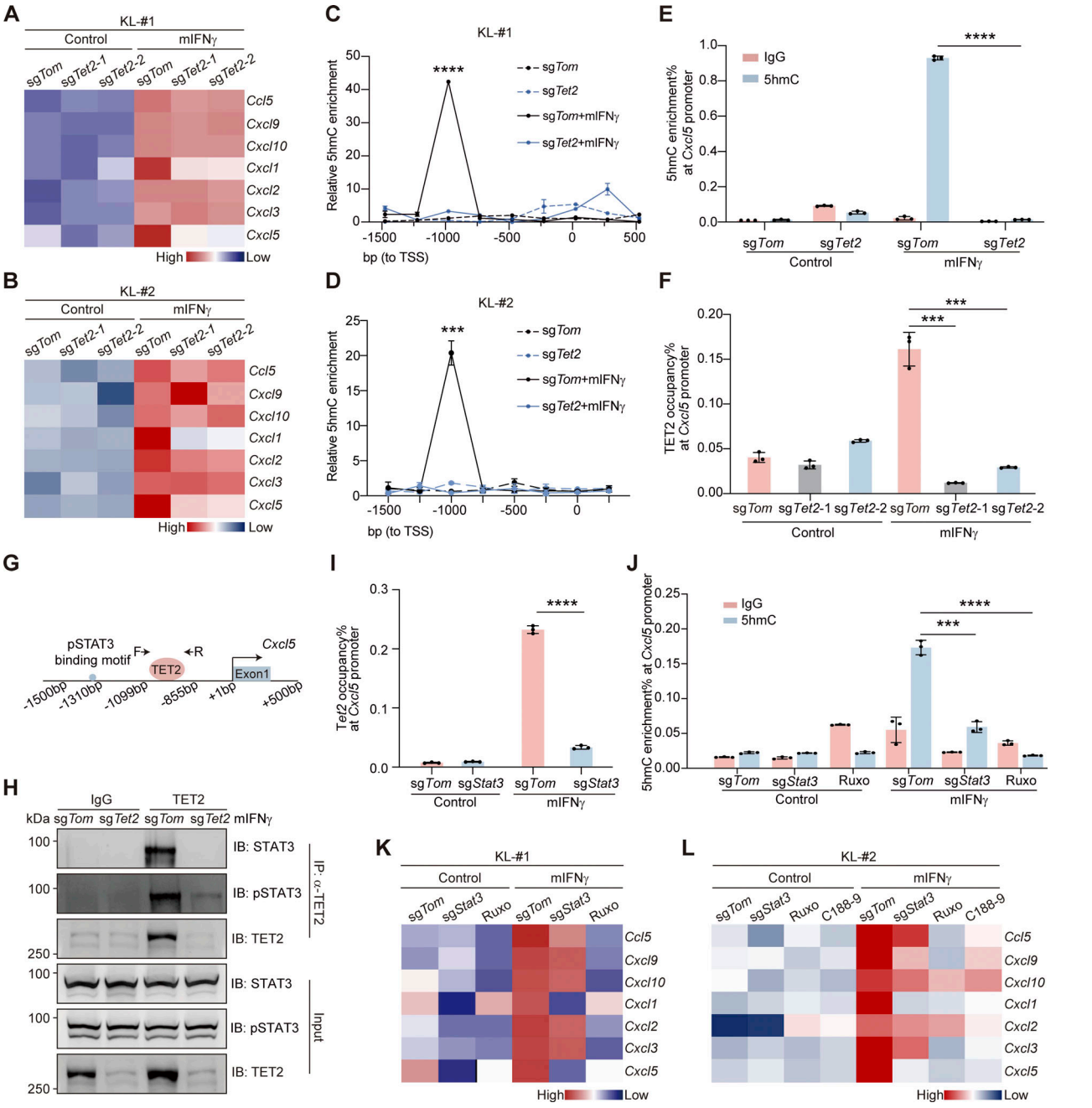


Figure 3. **TET2 interacts with STAT3 to transactivate *Cxcl5*. (A and B)** Heatmap of CXCL subfamily gene expression upon mIFNγ stimulation with or without *Tet2* KO in KL-#1 (A) or KL-#2 cells (B). Cells were treated with 150 ng/ml mIFNγ for 24 h before RT-qPCR. **(C and D)** The 5hmC enrichment at the *Cxcl5* promoter region was determined by hMeDIP-qPCR in KL-#1 (C) or KL-#2 cells (D). **(E)** The 5hmC enrichment at the *Cxcl5* promoter region was determined by hMeDIP-qPCR in *Tet2* KO KL cells. IgG was included as negative control. **(F)** *Tet2* occupancy at *Cxcl5* promoter region was determined by ChIP-qPCR in *Tet2* KO KL cells. **(G)** Schematic illustration of *Cxcl5* proximal promoter region, cis-regulatory elements, pSTAT3 binding motif, and binding of *Tet2*, as determined by ChIP assay. **(H)** The STAT3-TET2 interaction was confirmed by co-IP assay in KL-#1 cell line. Parallel blots using the same samples. IB, immunoblot. **(I)** *Tet2* occupancy at *Cxcl5* promoter region was determined by ChIP-qPCR in *Stat3* KO KL cells. **(J)** 5hmC enrichment at the *Cxcl5* promoter region was determined by hMeDIP-qPCR in *Stat3* KO KL cells and Ruxo (2 μM)-treated KL cells. IgG was included as the negative control. **(K)** Heatmap of CXCL subfamily genes expression upon mIFNγ stimulation, *Stat3* KO, and/or Ruxo treatment (2 μM) in KL-#1 cells. **(L)** Heatmap of CXCL subfamily gene expression upon mIFNγ stimulation, *Stat3* KO, Ruxo treatment (2 μM), or C188-9 treatment (5 μM) in KL-#2 cells. Data in A–F and H–L represent one experiment of three independent repeats. ***P < 0.001, ****P < 0.0001 by one-way ANOVA test (C–F, I, and J). Data are represented as mean ± SD. Source data are available for this figure: SourceData F3.

TG is degraded via hydrolysis, a process catalyzed by adipose triglyceride lipase (ATGL), which can be activated by abhydrolase domain containing 5 (ABHD5) and suppressed by cell death inducing DFFA-like effector C (CIDEC), hypoxia inducible lipid droplet associated (HILPDA), and G1/G1 switch 2 (G0S2) (Nielsen et al., 2014) (Fig. S5 M). We then examined these genes related to TG hydrolysis in isolated neutrophils from KL-ADC and KL-SCC. We found the most significant changes were

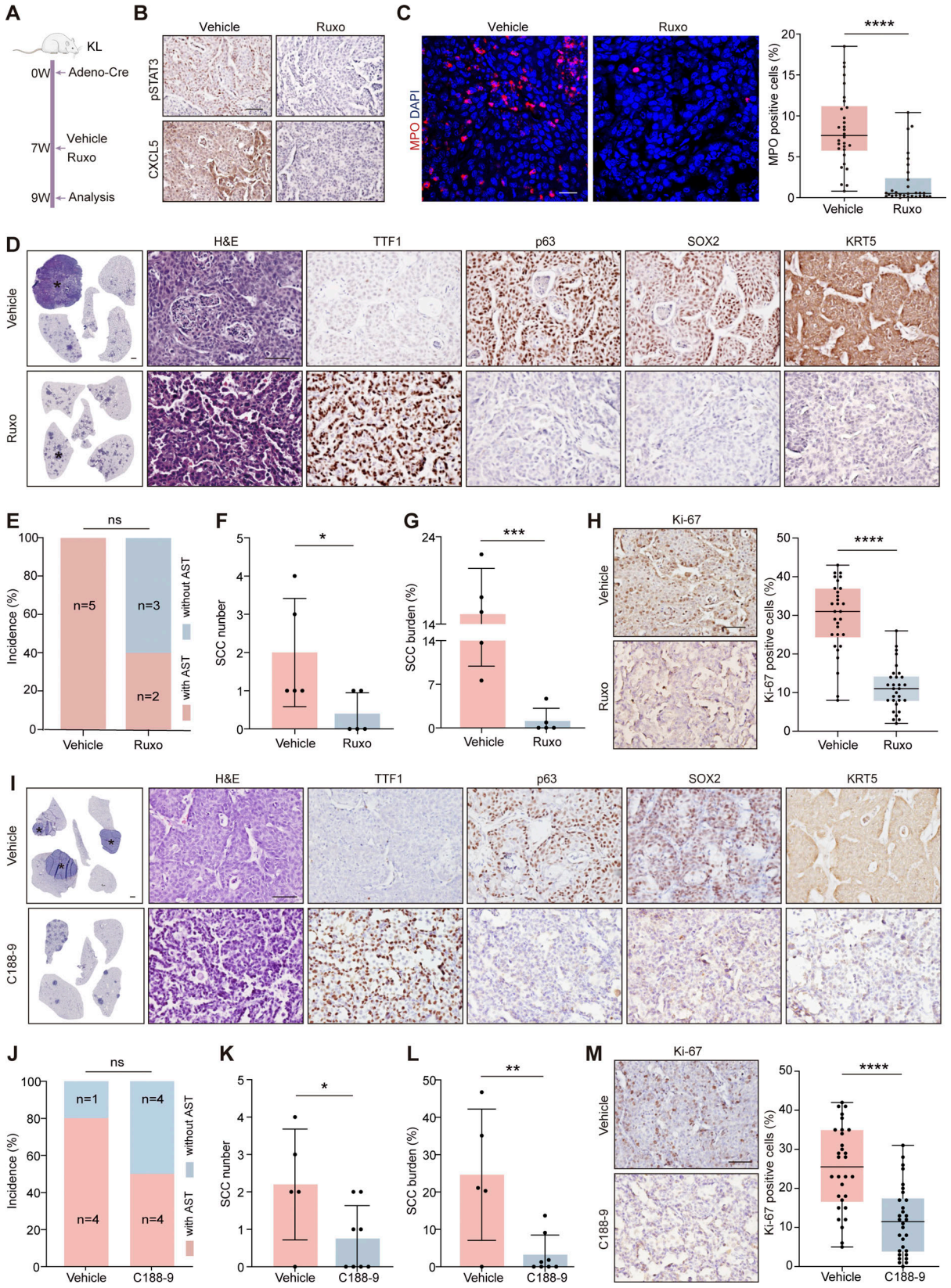


Figure 4. **Targeting STAT3 suppresses CXCL5 production, neutrophil infiltration, and AST in *KL* model. (A)** Schematic illustration of Ruxo treatment mouse experiment. W, week. **(B)** Representative IHC staining for pSTAT3 and CXCL5 in *KL* mice treated with vehicle and Ruxo. Scale bar: 50 μm. **(C)** Representative fluorescence staining of neutrophil (MPO-positive cells) infiltration in *KL* tumors. red: MPO; blue: DAPI. Statistical analyses are shown on the right. Scale bar: 20 μm. The statistical fields include both ADC and SCC pathologies. 30 representative images for each group were counted. **(D)** Representative H&E staining and IHC staining in *KL* mice treated with vehicle or Ruxo. The whole lungs are reused in Fig. S4 K. * indicates SCC. Scale bar for whole lung: 1 mm; scale

bar for others: 50 µm. **(E–G)** Statistical analyses of the AST incidence (E), the number (F), and burden (G) of SCC in *KL* model treated with vehicle ($n$ = 5) or Ruxo ($n$ = 5). **(H)** Representative Ki-67 IHC staining and statistical analyses. Scale bar: 50 µm. 30 representative images for each group were counted. **(I)** Representative H&E staining and IHC staining in *KL* mice treated with vehicle or C188-9. The whole lungs are reused in Fig. S4 L. * indicates SCC. Scale bar for whole lung: 1 mm; scale bar for others: 50 µm. **(J–L)** Statistical analyses of the AST incidence (J), the number (K), and burden (L) of SCC in *KL* model treated with vehicle ($n$ = 5) or C188-9 ($n$ = 8). **(M)** Representative Ki-67 IHC staining and statistical analyses. Scale bar: 50 µm. 30 representative images for each group were counted. Data in B–M represent one experiment of two independent repeats. *P < 0.05, **P < 0.01, ***P < 0.001, ****P < 0.0001 by two-tailed unpaired Student's $t$ test (C, F–H, and K–M), Fisher's exact test (E and J). ns: not significant. Data are represented as mean ± SD.

downregulation of *Atgl* expression and upregulation of *Hilpda* and *G0s2* expression in KL-SCC–derived neutrophils (Fig. S5 N). Hence, these findings indicate that lipid accumulation seen in SCC is likely attributed to dysregulated TG hydrolysis in neutrophils.

We next tested if EIPA administration could inhibit AST in GEMM. We treated the *KL* model with EIPA for 2 wk and found that EIPA treatment dramatically blocked lipid transport (Fig. 6, A and B) and suppressed squamous transition in *KL* mice (Fig. 6 C and Fig. S5 O). EIPA treatment almost blocked squamous transition in *KL* mice and the majority of tumors exhibited ADC pathology with high TTF1 expression and no p63, SOX2, and KRT5 expression (Fig. 6 C). The AST incidence, the number, and burden of SCC were also decreased by EIPA treatment (Fig. 6, D–F). Consistently, Ki-67 staining data revealed that cell proliferation was also decreased in EIPA-treated *KL* tumors (Fig. 6 G). These data together support that the blockage of neutrophil–cancer cell lipid transfer can serve as a potential strategy for overcoming AST.

## Discussion

Previous studies have identified TET2 as an important tumor suppressor in myeloid cancers as well as solid cancer (Delhommeau et al., 2009; Langemeijer et al., 2009; Lian et al., 2012; Xu et al., 2022). Interestingly, our work here demonstrates that TET2 is required for squamous transition in the *KL* model and *Tet2* KO significantly promotes *KL* mouse survival, indicative of a potential benefit to target TET2 in this specific subtype of lung cancer. Lung cancer is known to harbor strong phenotypic plasticity and display histological transformation from ADC to SCC or small cell lung cancer, which is frequently associated with malignant progression and drug resistance (Chen et al., 2021; Quintanal-Villalonga et al., 2021a, 2021b). Our previous work has revealed that *Tet2* KO promotes *Kras*-driven lung cancer growth in GEMM (Xu et al., 2022). Consistently, we found that *Tet2* KO also promotes the growth of KL-ADC. Of note, our data clearly demonstrated that KO of *Tet2* impairs squamous transition in the *KL* model. Hence, in the *LKB1*-deficient context, TET2 seems important for sustaining lung cancer plasticity. We reason such functional differences of TET2 might be genetic context dependent, similar to our previous finding about the dual function of YAP in lung cancer (Zhang et al., 2015b; Gao et al., 2014). Future work is interesting to clarify the detailed mechanisms behind these observations.

Previous functional and mechanistic studies of TET2 mainly focused on immune cells (Cong et al., 2021; Zhang et al., 2015a; Banks et al., 2021). For example, in dendritic cells, TET2 interacts with STAT3 to transactivate *IL-6/10* (Català-Moll et al., 2022). In macrophages, TET2 can interact with RelA to transactivate NF-κB target genes (Chen et al., 2022). In B cells, TET2 restrains IL-10 production and thereby promotes liver cancer progression (Lu et al., 2022). Except for immune cells, TET activity-dependent epigenetic pathway can increase the global 5hmC level and suppress the tumor progression of melanoma and prostate cancer (Lian et al., 2012; Zhao et al., 2020). We here find that TET2 is recruited by STAT3 to *CXCL5* promoter region for transcriptional activation. Although both CXCL3 and CXCL5 are classical chemokines for recruiting neutrophils into tumor microenvironment (Mollaoglu et al., 2018), only *CXCL5* is transcriptionally regulated by TET2. Although we can't conclusively exclude the involvement of *CXCL3* through protein-level analyses and there might exist other TET2-independent mechanisms involved in *CXCL3* gene regulation, our data support an important role of CXCL5 in neutrophil recruitment during the AST process. Previous study shows that SOX2 or NKX2-1 directly regulates *CXCL5* gene expression. Interestingly, SOX2 is known to activate *STAT3* and the latter could promote *CXCL5* gene expression (Mollaoglu et al., 2018; Traber et al., 2015), indicative of another potential indirect regulatory loop involved in *CXCL5* regulation by SOX2. Moreover, STAT3 can also bind to TET2 to regulate downstream inflammatory signaling (Català-Moll et al., 2022). We demonstrate here that TET2 promotes *CXCL5* gene expression potentially through STAT3. It seems that multiple regulatory loops might be involved in *CXCL5* transcriptional regulation. Besides, our work further shows that anti-CXCL5 could effectively reduce neutrophil infiltration and inhibit AST. While the use of saline, rather than an appropriate IgG subtype, as the control is the caveat for the anti-CXCL5 treatment experiment, similar results are observed from the CRISPR/Cas9-mediated *Cxcl5* KO experiment, underscoring the important role of CXCL5 in neutrophil recruitment and AST. Approaches targeting the STAT3 pathway are well-explored both preclinically and clinically, e.g., C188-9 is applied in preclinical models of inflammatory bowel disease and solid cancer (Kasembeli et al., 2018; Jung et al., 2017; Pan et al., 2022), and Ruxo has been approved for the treatment of patients with myelofibrosis, polycythemia vera, and steroid-refractory acute graft-versus-host disease treatment (Huynh et al., 2019; Wong et al., 2017; Ajayi et al., 2018; Lussana et al., 2018; Modi et al., 2019). Our data show that targeting STAT3 efficiently inhibits CXCL5 production, neutrophil infiltration, and AST in the *KL* model. Moreover, we find a dramatic suppression of *KL* cancer progression after Ruxo or C188-9 treatment, highlighting the potential benefit of JAK-STAT targeting strategy. One limitation of our study is that we didn't perform mouse survival analyses in the experiments targeting CXCL5 or STAT3. Thus, it is currently unclear whether these intervention strategies targeting AST

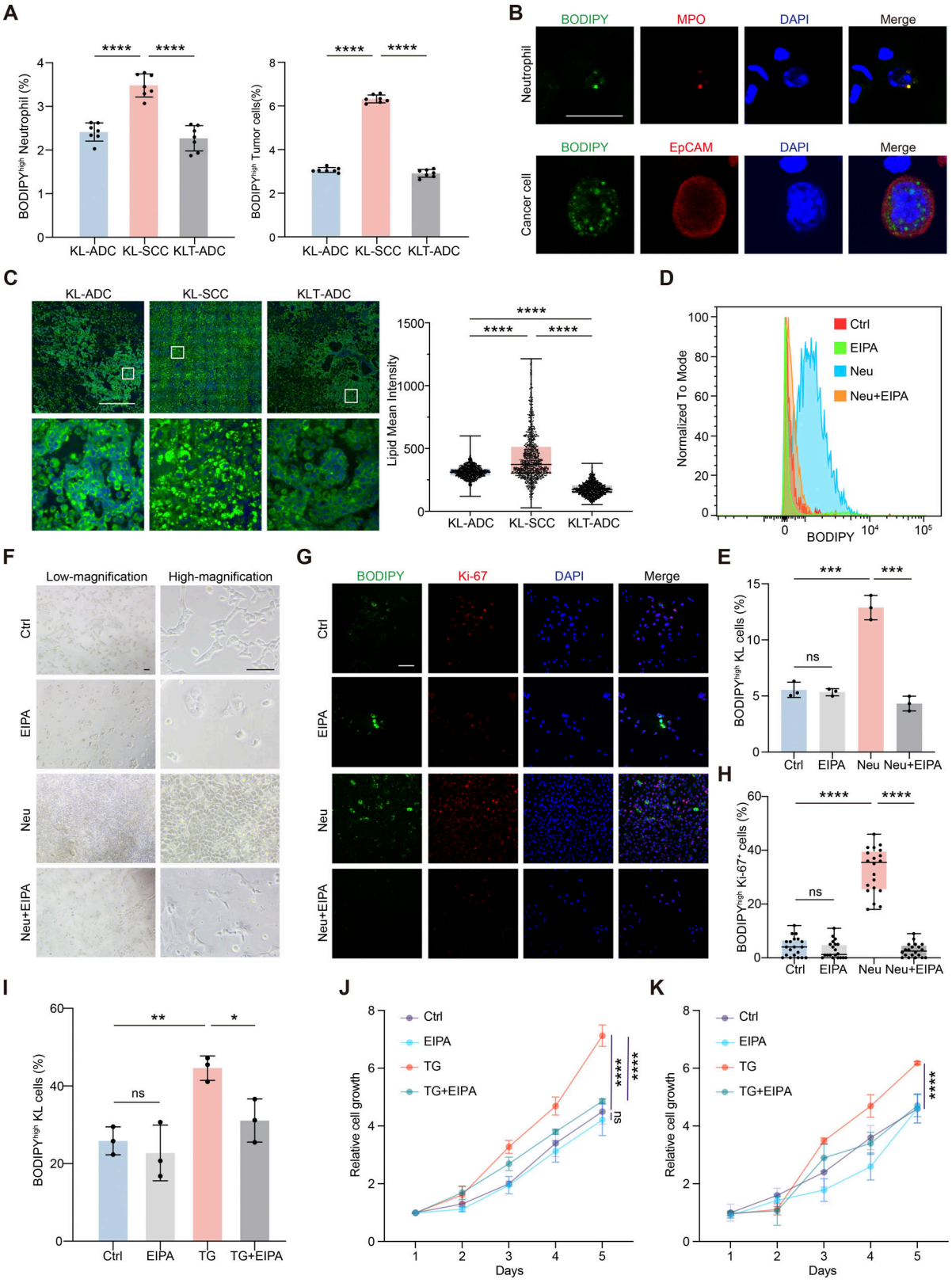


Figure 5. **Lipid-laden neutrophils transfer lipid to *KL* tumors to fuel AST. (A)** Statistical analyses of lipid levels in neutrophils and tumor cells isolated from KL-ADC ($n$ = 7), KL-SCC ($n$ = 7), and KLT-ADC ($n$ = 7) tumors. **(B)** Representative fluorescence staining showing the colocalization of lipid (BODIPY) with the neutrophils (MPO) or cancer cells (EpCAM) isolated from KL-SCC. Scale bar: 10 μm. **(C)** SRS microscope analysis for lipid level in KL-ADC, KL-SCC, and KLT-ADC. The top row is formed by merging 100 smaller images, respectively. Statistical analyses are shown on the right. 900 representative images for each group were counted. Lipid and protein signals were indicated as green and blue, respectively. Scale bar: 500 μm. **(D and E)** (D) KL cells were co-cultured with neutrophils isolated from KL-SCC. EIPA was added to block lipid transport. Lipid levels of KL cells were quantitated by FACS and statistical analyses are shown

(E). **(F)** Cell morphology of KL-#1 cells mono-cultured (Ctrl) or co-cultured with neutrophils (Neu) isolated from KL-SCC. EIPA was added to block lipid transport (Neu+EIPA). Scale bar: 100 µm. **(G and H)** (G) Representative fluorescence staining of BODIPY and Ki-67 in KL-#1 cells co-cultured with neutrophils. Scale bar: 100 µm. Statistical analyses are shown (H). 20 representative images for each group were counted. **(I)** KL cells were treated with TG-micelles (0.1 mM). EIPA was added to block TG transport. Lipid levels of KL cells were quantitated by FACS. **(J and K)** Relative growth of KL-#1 (J) or KL-#2 (K) cells after treatment with TG-micelles (0.1 mM). Cells in sextuplicate were treated with drugs over the entire experiment, with relative cell growth determined daily and normalized to day 0. Data in A–K represent one experiment of three independent repeats. *P < 0.05, **P < 0.01, ***P < 0.001, ****P < 0.0001 by one-way ANOVA test (A, C, E, and H–K). ns: not significant. Data are represented as mean ± SD.

would benefit the mice in the long run. Nonetheless, our findings might provide a potential strategy to treat those patients with high risk for AST, which requires future detailed study.

Previous studies have highlighted the promotive role of tumor-infiltrating neutrophils in AST with unclear mechanisms (Koyama et al., 2016; Mollaoglu et al., 2018). Our data show that the neutrophils infiltrated into SCC are laden with increased lipid, with TG as the major component. Dysregulated TG hydrolysis is observed in neutrophils infiltrated into SCC, which might partially explain the increased lipid load. TG is important for energy storage and has previously been implicated in diverse pathological processes including inflammation and cancer (Wang and Dubois, 2010; Spiegelman and Flier, 2001). Interestingly, we found that lung neutrophils transfer TG to squamous cancer for promoting cell proliferation. Blockage of lipid transport by EIPA almost completely blocks AST and tumor malignant progression. These findings suggest that EIPA treatment has the capability to inhibit lipid transfer both in vitro and in vivo. While we cannot exclude the possibility that EIPA treatment may have a cytotoxic effect, our data indicate that the dose of EIPA we used did not significantly affect the KL cell proliferation. Importantly, this provides another potential strategy to inhibit AST from the metabolic communication aspect.

It's worth noting that multiple AST or SCC mouse models have been established previously (Perera et al., 2009; Xiao et al., 2013; Mukhopadhyay et al., 2014; Xu et al., 2014; Liu et al., 2015, 2019; Camolotto et al., 2018; Mollaoglu et al., 2018; Ruiz et al., 2019; Ferone et al., 2016; Tata et al., 2018). It'll be interesting to check if our mechanistic findings also apply to various models based on the strong link between neutrophils and squamous pathology. Similarly, it'll be interesting to test our targeting strategies proposed here in various AST or SCC models. Somerville et al. have previously suggested a link between neutrophils and squamous transition in pancreatic cancer (Somerville et al., 2020). Future studies would be interesting to test if the contribution of lipid transfer to squamous transition we identified here can be applied to other cancer types. Besides neutrophils, we also found a significant increase of TAM upon *Tet2* KO in the *KL* model, which might require future efforts to clarify its potential contribution to AST.

In summary, our work here identifies TET2 as an important regulator of AST and unveils a novel mechanism by which TET2–STAT3–CXCL5 nexus promotes lipid-laden neutrophil recruitment to facilitate AST (Fig. 6 H). We provide proof-of-principle for developing therapies targeting the TET2–STAT3–CXCL5 nexus and/or the lipid transport from tumor-associated neutrophils. Further investigations are warranted to confirm these findings, especially in clinical samples, and to prospectively evaluate the effect of the above-mentioned potential therapeutic strategies on overcoming squamous transition.

## Materials and methods

### Mouse study

*Kras*$^{LSL\text{-}G12D/+}$, *Lkb1*$^{L/L}$, and *Tet2*$^{L/L}$ C57BL/6 mice were generously provided by Dr. Tyler Jacks (Jackson et al., 2001), Ronald Depinho (Bardeesy et al., 2002), and Guoliang Xu (Dai et al., 2016), respectively. All mice were kept in a specific pathogen–free environment of the Center for Excellence in Molecular Cell Science and treated in strict accordance with protocols (SIBCB-2101008) approved by the Institutional Animal Care and Use Committee of the Shanghai Institutes for Biological Sciences, Chinese Academy of Sciences. Mice at 6–8 wk of age were treated with Adeno-Cre ($2 \times 10^6$ p.f.u.) via nasal inhalation and analyses were performed after 10 wk. Mice at 6–8 wk of age were treated with lentivirus ($2 \times 10^5$ p.f.u.) via nasal inhalation and pathological analyses were performed 24 wk afterward.

Ruxo (HY-50856; MedChemExpress), C188-9 (HY-112288; MedChemExpress), or EIPA (HY-101840; MedChemExpress) were formulated in 10% DMSO, 40% PEG300, and 50% saline. CXCL5-neutralizing antibody (αCXCL5) (mab433; R&D) was formulated in 50% saline. Treatment of Ruxo (45 mg/kg) and vehicle (10% DMSO: 40% PEG300: 50% saline) was conducted daily for 2 wk through intraperitoneal injection in *KL* mice, as previously reported (Siersbæk et al., 2020). Treatment of C188-9 (75 mg/kg) was conducted daily for 2 wk through intraperitoneal injection in *KL* mice as previously described (Zhao et al., 2021). Treatment of αCXCL5 (5 mg/kg) and saline was conducted weekly for 2 wk through intraperitoneal injection in *KL* mice, as previously reported (Li et al., 2020b). Treatment of EIPA (10 mg/kg) was conducted daily for 2 wk through intraperitoneal injection in *KL* mice, as previously reported (Li et al., 2020a). Mice were then sacrificed for histopathological examination. Tumor incidence and number and burden were analyzed using ImageJ software as previously described (Chen et al., 2021). All treatment experiments were conducted using littermate mice as controls.

### CRISPR-Cas9 plasmids construction and lentivirus production

Single guide RNAs (sgRNAs) against *Tet1*, *2*, or *3* were previously described (Zuo et al., 2017). We employed the CRISPR-related plasmid pSECC for lentivirus packaging and delivered it via nasal inhalation to KL mice, achieving targeted gene KO in vivo as previously reported (DuPage et al., 2009). For in vivo viral infection, lentivirus supernatant was collected 48 h after

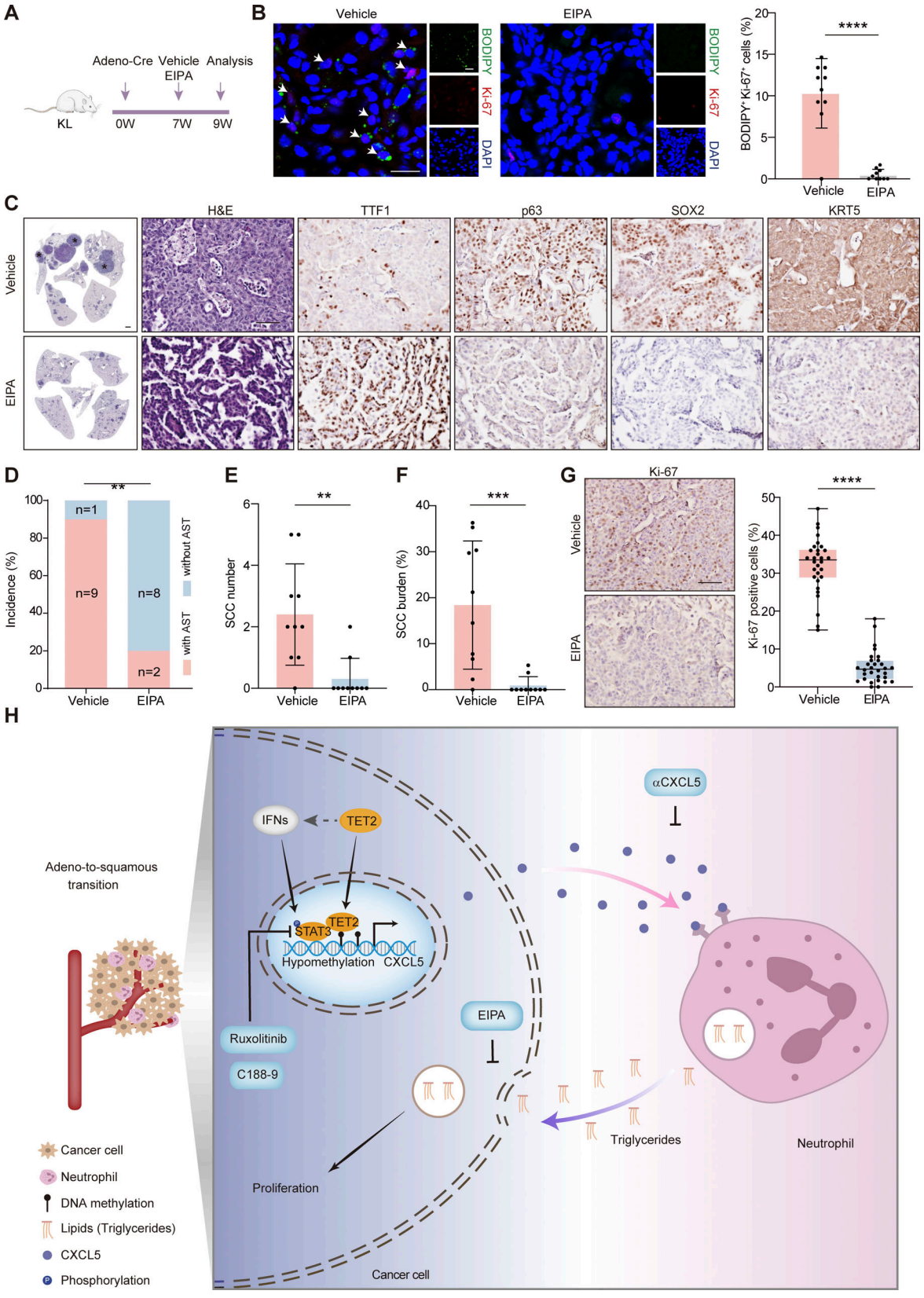


Figure 6. **Blockage of neutrophil-derived lipid transport suppresses AST in *KL* model. (A)** Schematic illustration of EIPA treatment mouse experiment. W, week. **(B)** Representative BODIYP and Ki-67 fluorescence staining of *KL* tumors. Red: Ki-67; green: BODIPY; blue: DAPI. Scale bar: 20 μm. Statistical analyses are shown on the right. Arrows show BODIPY and Ki-67 double-positive cells. 10 representative images for each group were counted. **(C)** Representative H&E and IHC staining in *KL* tumors. The whole lungs are reused in Fig. S5 Q. * indicates SCC. Scale bar for whole lung: 1 mm; scale bar for others: 50 μm. **(D–F)** Statistical analyses of the AST incidence (D), the number (E), and burden (F) of SCC in *KL* mice treated with vehicle ($n$ = 10) or EIPA ($n$ = 10). **(G)** Representative Ki-67 IHC

staining and statistical analyses. Scale bar: 50 μm. 30 representative images for each group were counted. **(H)** Working model for TET2-mediated AST. In KL tumor cells, TET2 is recruited by STAT3 to CXCL5 promoter region and transcriptionally upregulates CXCL5, which in turn promotes infiltration of lipid-laden neutrophils to facilitate AST. Targeting the TET2–STAT3–CXCL5 nexus and/or the lipid transport could serve as potential therapeutic strategies to inhibit AST in lung cancer. Data in B–G represent one experiment of two independent repeats. **P < 0.01, ***P < 0.001, ****P < 0.0001 by two-tailed unpaired Student's *t* test (B and E–G), Fisher's exact test (D). Data are represented as mean ± SD.

transfection and concentrated by ultracentrifugation at 20,000 rpm for 2 h and resuspended overnight in an appropriate volume of OptiMEM (Gibco). All sgRNAs were as follows: sg*Tomato*, 5′-GGCCACGAGTTCGAGATCGA-3′; sg*Cxcl5*, 5′-ATGGCGAGATGGAACCGCTG-3′; sg*Tet1*-1, 5′-GGCATGCTGGACTTCATTCT-3′; sg*Tet1*-2, 5′-GATGTCCATGCCGGTTACAC-3′; sg*Tet1*-3, 5′-GAAGCCAGAGGCCACCTCAC-3′; sg*Tet2*-1, 5′-CAGGGAGCAAGAGATTCCGA-3′; sg*Tet2*-2, 5′-TCAGTCCTCCACTCTCAGAC-3′; sg*Tet2*-3, 5′-GTGAACCAAGGACCGTCTCC-3′; sg*Tet3*-1, 5′-CCCTACTTCCACAGAGCCTC-3′; sg*Tet3*-2, 5′-GCCTGTTAGGCAGATTGTTC-3′; sg*Tet3*-3, 5′-ACAAGCTGGAGGAGCTCATC-3′; and sg*Stat3*, 5′-GATCGTGGCCCGATGCCTGT-3′. Primers used for detecting sgRNA efficiency were as follows: sg*Tet1* test-F, 5′-AGCCTCCAAACACAGTTGCT-3′; sg*Tet1* test-R, 5′-TGGCTATGTCTGAGGAAGCG-3′; sg*Tet2* test-F, 5′-ATGATTGTGGCTCACCGAGC-3′; sg*Tet2* test-R, 5′-GTCTCTGTGGCCTGTTGACT-3′; sg*Tet3* test-F, 5′-GGCAGAACTGGAGCAGCTAT-3′; sg*Tet3* test-R, 5′-GGTGTGAGTGGGTTCTCAGC-3′.

Genotyping primers used for detecting *Tet2* KO were as follows: *Tet2*-C, 5′-ACACAGAGAAAAGGGTACGTGAA-3′; *Tet2*-F, 5′-ACTCATTAGTGAAATATGTGAGTG-3′; *Tet2*-R, 5′-CTGCTTAGTTCAATGCCAACC-3′.

### Histologic, IHC, and IF analyses

Lung tissues were freshly dissected and fixed with 10% formalin buffer and then embedded in paraffin and cut into 5-μm sections. Hematoxylin and Eosin (H&E) staining, and IHC and IF staining were performed as described previously (Wang et al., 2021). For IHC staining, the stained sections were evaluated using H-score as previously described (Detre et al., 1995; Wang et al., 2019). In brief, staining intensity was scored in the following categories: negative staining (scored as 0), weak positive staining (scored as 1), intermediate positive staining (scored as 2), and strong positive staining (scored as 3). The IHC score was calculated with the formula: cell percentage × staining intensity score ×100. The final IHC score was on a scale of 0–300. To calculate the percentages of cells positive for Ki-67 or MPO and the relative scores for 5mC or 5hmC, at least 30 high-power fields were randomly selected from each group for statistical analysis as previously described (Li et al., 2015). IF images were captured using the laser confocal microscope with a Leica TCS SP8 system with an HC PL APO CS2 63x/1.40 OIL objective as previously described (Guo et al., 2022). The following antibodies used for IHC and IF: TTF1 (ab133638; Abcam), p63 (ab124762; Abcam), SOX2 (ab92494; Abcam), Cytokeratin 5 (KRT5) (BS1208; Bioworld), 5mC (BI-MECY-0100; Eurogentec), 5hmC (39792; Active Motif), Ki-67 (NB500; Novus), pSTAT3 (9145; CST), MPO (AF3667; R&D system), BODIPY (GC42959; GLPBIO), EpCAM (2929; CST), and DAPI (4083; CST).

### Western blot

Tissues or cell lysates were prepared for western blot analysis with the following antibodies: TTF1 (ab133638; Abcam), p63 (12143-I-AP; Proteintech), Cytokeratin 5 (KRT5) (BS1208; Bioworld), TET2 (18950S; CST), STAT3 (9132; CST), pSTAT3 (9145; CST), and β-actin (AC026; ABclonal).

### Real-time qPCR (RT-qPCR)

Total RNA was isolated by TRIzol reagent and retrotranscribed into first-strand cDNA using the first-strand synthesis kit (Invitrogen). cDNA was subjected to RT-qPCR with SYBR-Green Master PCR mix (Roche). Primers used for RT-qPCR were as follows: *Tet2*, 5′-GCTCCAATATACAAGAAGCTTGCAC-3′ and 5′-TATTGAGGGTGACCACCACTGTACT-3′; *p63* (*DNp63*), 5′-ATGTTGTACCTGGAAAACAATG-3′ and 5′-GATGGAGAGAGGGCATCAAA-3′; *Sox2*, 5′-CACAACTCGGAGATCAGCAA-3′ and 5′-TCCGGGAAGCGTGTACTT-3′; *Krt5*, 5′-CAGAGCTGAGGAACATGCAG-3′ and 5′-CATTCTCAGCCGTGGTACG-3′; *Krt14*, 5′-ATCGAGGACCTGAAGAGCAA-3′ and 5′-TCGATCTGCAGGAGGACATT-3′; *Abhd5*, 5′-TGGTGTCCCACATCTACATCA-3′ and 5′-CAGCGTCCATATTCTGTTTCCA-3′; *Atgl*, 5′-GGATGGCGGCATTTCAGACA-3′ and 5′-CAAAGGGTTGGGTTGGTTCAG-3′; *Cidec*, 5′-ATGGACTACGCCATGAAGTCT-3′ and 5′-CGGTGCTAACACGACAGGG-3′; *Hilpda*, 5′-TGCTGGGCATCATGTTGACC-3′ and 5′-TGACCCCTCGTGATCCAGG-3′; *G0s2*, 5′-GTGAAGCTATACGTGCTGGG-3′ and 5′-CCGTCTCAACTAGGCCGAG-3′; *Actin*, 5′-CAGCCTTCCTTCTTGGGTAT-3′ and 5′-GGTCTTTACGGATGTCAACG-3′.

### RNA-sequencing (RNA-seq) data analyses

RNA-seq data of mouse KL lung tumors were obtained from our previous study (GSE78220) (Fang et al., 2023). RNA-seq data were aligned to mouse genome reference using STAR (v2.6.0) (Dobin et al., 2013). To comparatively analyze the gene expression, RNA-seq data of TCGA-LUAD (tumor: $n$ = 526, normal: $n$ = 59) and TCGA-LUSC (tumor: $n$ = 550, normal: $n$ = 49) were downloaded from UCSC Xena (https://xenabrowser.net), from which samples with tumor purity >0.5 were used (Aran et al., 2015) (LUAD: $n$ = 430, LUSC: $n$ = 433). Combat function in the SVA package was used to correct the batch effects (Leek et al., 2012). "GSVA" package was used to evaluate the expression scores of signal pathways (Hänzelmann et al., 2013).

### Establishment of primary cell lines

To obtain the primary cell line of $Kras^{G12D}$; $Lkb1^{-/-}$, lung tumor tissues from $Kras^{LSL\text{-}G12D/+}$; $Lkb1^{L/L}$ mice infected with Adeno-Cre were isolated in a sterile manner. Tissues were washed extensively with 1× PBS with 200 μg/ml penicillin (Sigma-Aldrich) and 200 μg/ml streptomycin (Sigma-Aldrich). Next, tissues were mechanically dissociated using a scalpel with removal of

vascular material and plated in RPMI (Gibco) with 10% FBS, penicillin/streptomycin for further experiments.

### Establishment of squamous organoids

To obtain the squamous organoids, the tissues of KL-SCC were mechanically dissociated using a scalpel and digested with collagenase Type 1 (LS004196; Worthington-Biochem). Then single cells were mixed with matrigel and plated in mouse medium as previously described (Hu et al., 2018). The full-length wild-type or inactive mutant ($H_{1295}R_{1296}D_{1297}$ mutated to $Y_{1295}R_{1296}A_{1297}$) (Xu et al., 2022) *Tet2* was overexpressed in SCC organoid cells as previously described (Hai et al., 2020).

### hMeDIP-qPCR analysis

The hMeDIP-qPCR assay was performed as previously described (Ito et al., 2010). Briefly, genomic DNA was collected (2 µg) and denatured, sonicated for 15 min (70% power, 30 s on, 30 s off; Bioruptor), and immunoprecipitated with anti-5hmC (39769; Active Motif) or IgG antibody (DA1E; CST) for 3.5 h. The antibody–DNA complexes were pulled down using protein G beads (17061801; GE) for 1.5 h. Beads were washed three times and treated with proteinase K (TaKaRa) at 65°C for 4 h. DNA was isolated by PCR Purification Kit (QIAGEN) and analyzed by RT-qPCR using the primers as follows: *Cxcl5*-1, 5′-AAGTTCGAAAGT CTACCACC-3′ and 5′-GTGGTGCCCTGGCTTTCTTT-3′; *Cxcl5*-2, 5′-GTTATAACCGACTGCCTTGG-3′ and 5′-CAGCTGAGGGAC TCATCCGT-3′; *Cxcl5*-3, 5′-CACCAACCTCCTTTAGCTTC-3′ and 5′-TAAAAGCTGCTTACTGGAAG-3′; *Cxcl5*-4, 5′-GAAGGCCAT TCATGCAGCTG-3′ and 5′-CGAAGACTGTTTTTATTCAG-3′; *Cxcl5*-5, 5′-CACACATTTCAAATGTATTT-3′ and 5′-ACCTGGGAG ATGGCTCAACC-3′; *Cxcl5*-6, 5′-GTCAGCAATAGTGTTTGTAG-3′ and 5′-GAGTGGCTCTTTGCCAAATC-3′; *Cxcl5*-7, 5′-TCCTAGCCA TCCTCCCGCCC-3′ and 5′-CTCATTGTGGACAAGATCCC-3′; *Cxcl5*-8, 5′-CCTCCAGCTCCGCAGCTCCG-3′ and 5′-AAGGGGCAG CTGTGGAAGAG-3′; and *Cxcl5*-9, 5′-CCTCAGTCATAGCCGCAA CG-3′ and 5′-GAGGATGCACAGGTGAGCCC-3′.

### ChIP-qPCR assays

ChIP-qPCR assay was performed as previously described (Lan et al., 2007). Briefly, cells were crosslinked with 1% paraformaldehyde for 10 min and stopped by glycine. The chromatin was sonicated for 30 min (30% power, 30 s on, 30 s off; Bioruptor) and immunoprecipitated with anti-TET2 antibody (Shanghai Youke) or IgG for 3.5 h as previously described (Chen et al., 2018). The antibody–chromatin complexes were pulled down using protein A beads for 1.5 h. Beads were washed three times with high salt buffer, two times with low salt buffer, and once with TE buffer. After crosslink reversal and proteinase K (TaKaRa) treatment, DNA was isolated by PCR Purification Kit (QIAGEN) and analyzed by RT-qPCR.

### Co-IP

KL cells were washed with cold PBS and lysed in NP-40 buffer containing 50 mM Tris-HCl (pH 7.4), 300 mM NaCl, 0.5% NP-40, and protease inhibitor cocktail (Biotool) with rotation at 4°C for 45 min. Then the cell lysate was centrifuged at 13,000 rpm for 15 min and the supernatant was incubated with IgG antibody (DA1E; CST) or TET2 antibodies (18950S; CST) for 2.5 h, followed by incubation with Protein A for another 1.5 h at 4°C. Beads were washed three times with cold NP-40 buffer and the proteins were denatured by SDS loading buffer containing dithiothreitol.

### ELISA

Tumors derived from *KL* and *KLT* mice at 7 wk after Adeno-Cre infection were randomly collected in different volumes of cell lysis buffer according to their weight. Then, the whole tumor extract was centrifuged at 14,000 rpm for 15 min and the supernatant was collected. The level of CXCL5 was detected in eight tumors in each group using a mouse CXCL5 ELISA kit according to the manufacturer's instructions.

### Co-culture KL cells with neutrophils

Freshly isolated neutrophils from KL-SCC by FACS and KL cells were mixed and then seeded in 12-well plates with 10% FBS/DMEM medium in a direct cell–cell contact manner (the ratio of neutrophils to KL cells was 20:1). EIPA (50 µM) was added to block the lipid transport. For lipid analysis in KL cells by FACS, all cells were cultured for 24 h and then stained with BODIPY 493/503 (GC42959; GLPBio) and EpCAM (563216; BD). For cell proliferation analysis in KL cells, all cells were cultured for 48 h and then stained with Ki-67 (NB500; Novus) and DAPI (4083; CST).

### SRS microscope analysis

In the setup of SRS microscope, the pulsed Stokes (1,040 nm) and pump (804 nm) beams were directed from a commercial optical parametric oscillator (80 MHz; Insight DS+), chirped by SF57 glass rods, coupled into an inverted laser-scanning microscope (FV1200; Olympus), and focused onto the tissue sections with an objective lens (UPLSAPO 60 × W, NA = 1.2; Olympus). The Stokes beam was modulated at 20 MHz by an electronic optic modulator. The forward-going pump and Stokes beams were collected by a high NA oil condenser (NA = 1.4) after passing through samples. Transmitted through a lowpass filter, the stimulated Raman loss signal was detected by a reverse-biased photodiode followed by demodulation with a lock-in amplifier (HF2LI; Zurich Instruments) to feed the analog input of the microscope to generate images. For the unmixing of the two chemical components, we first acquired SRS images at 2,845 $cm^{-1}$ and 2,930 $cm^{-1}$ (the vibration frequency of $CH_2$ and $CH_3$ bonds, respectively). The relative concentrations of protein ($a_P$) and lipid ($b_L$) could be decomposed by linear algebra with the preknowledge of their SRS spectra (He et al., 2017).

For lipid detection, the tissue cryosections (20 µm) of *KL* and *KLT* mice were analyzed with SRS microscope.

For lipid quantification, we analyzed based on SRS microscope images using the previously described method (Shi et al., 2018). Briefly, we first acquired SRS signals at 2,845 $cm^{-1}$ and 2,930 $cm^{-1}$ bearing the mixed signals of lipid and protein. We then used a linear combination of the two image channels with coefficients to decompose the amounts of the two macromolecules. The signals at 2,845 $cm^{-1}$ ($I_{2845}$) and 2,930 $cm^{-1}$ ($I_{2930}$) are linear combinations of lipid and protein concentrations ($CH_L$ and $CH_P$) with coefficients $a_L$, $a_P$, $b_L$, and $b_P$ as shown in the

equations below. The ratio between $a_L$ ($a_P$) and $b_L$ ($b_P$) was obtained from the SRS spectrum of standard lipid (protein) samples. $a_L$ and $b_P$ were set to 1, and the rest of the coefficients were scaled to their relative values. $CH_L$ and $CH_P$ were then calculated to represent the concentrations of lipid and protein, respectively. In this SRS method, the quantification of the protein signal serves as the reference. The 900 fields of tissue cryosections (20 µm) for each group were analyzed. The range of lipid signal intensities we could obtain was 0–2,000. A lipid signal intensity of 500 was used as the cutoff to define high- and low-lipid levels.

$$I_{2845} = a_L CH_L + a_P CH_P$$
$$I_{2930} = b_L CH_L + b_P CH_P$$

For qualitative analysis of lipid, the standard curves of TG (G107438; Aladdin), cholesterol (A90286; Innochem), PC (T19514; Topscience), PE (P856654; Macklin), PS (T21437; Topscience), and SM (S877036; Macklin) were analyzed and then six fields of KL-SCC tissue cryosections (20 µm) were detected with SRS microscopy. 300 high-power fields were randomly selected for score analyses using the formula similar to H-score: cell percentage × imaging intensity score ×100. The final score was on a scale of 0–300.

### TG-micelle preparation and treatment

TG-micelles were prepared as previously described (Dai et al., 2017) to obtain the final following concentration: 3 mg/ml (4.695 mM). In detail, we first dissolved 39 mg $mPEG_{5000}$-b-$PCL_{5000}$ and 39 mg TG in 3 ml tetrahydrofuran solution. The mixed solution was slowly added dropwise to 8 ml of ultrapure water at a suitable stirring speed. The emulsion was dialyzed against phosphate buffer (PBS) for 24 h by using a 3,500 g/mol molecular weight cutoff dialysis membrane to remove residual organic solvent. The final TG-micelles were made up to 3 ml and filtered through a 0.45-µm filter before use.

To evaluate TG-micelle effects in vitro, $5 \times 10^5$ cells per well were seeded into 12-well plates and starved for 3 h in basal medium (without FBS) after attachment. The TG-micelles (final concentration at 0.1 mM) were added into the basal medium. EIPA (50 µM) was added to block lipid transportation. After incubation for 24 h, KL cells were stained with BODIPY 493/503 (GC42959; GLPBio) and EpCAM (563216; BD). FACS (BD LSRII flow cytometer) was used to detect the lipid signal.

For cell proliferation detection, 3,000 cells were seeded in sextuplicate in 96-well plates and starved for 3 h in basal medium (without FBS) after attachment. Next, TG-micelles (0.1 mM) were added into the complete medium with FBS. EIPA (50 µM) was added to block lipid transport. The cells were stained with 3-(4,5-dimethyl-2-thiazolyl)-2,5-diphenyl-2-H-tetrazolium bromide and assessed with Epoch multivolume spectrophotometer system (570 nm/630 nm) at indicated time points.

### FACS analysis

To prepare the single-cell suspension from mouse whole lung tissues or ex vivo cultured cells, the samples were incubated with fluorescently labeled antibodies. All the antibodies are listed as follows: EpCAM (563216; BD), CD45 (563709; BD), CD3 (553062; BD), CD4 (553051; BD), CD8 (551162; BD), Ly6G (551460; BD), CD11B (550993; BD), F4/80 (565410; BD), CD49b (563063; BD), and Foxp3 (12-4771-82; eBioscience). The population of indicated immune cells was analyzed by using the BD LSRII flow cytometer and FlowJo software as described previously (Jin et al., 2022).

### Statistical analyses

Differences were compared using two-tailed unpaired Student's *t* test or one-way ANOVA. P value < 0.05 was considered statistically significant. Error bars were represented with SD. Differences in AST incidence were calculated by Fisher's exact test. Survival analysis was performed using the Kaplan Meier method as previously described (Wu et al., 2018).

### Online supplemental material

Fig. S1 shows heatmap of indicated gene expression from TCGA, additional IHC data of the *KL* model, and data from CRISPR/Cas9-mediated *Tet* (*Tet1/2/3*) gene KO model (related to Fig. 1). Fig. S2 shows validation of *Tet2* KO, the whole lung of the *KL* or *KLT* model, and the gene expression of squamous lineage markers (related to Fig. 1). Fig. S3 demonstrates that TET2 promotes neutrophil infiltration potentially through the upregulation of CXCL5 expression (related to Fig. 2). Fig. S4 shows validation of TET2/STAT3 inhibition in *KL* tumor cell lines, and additional data of Ruxo/C188-9 treatment in *KL* model (related to Figs. 3 and 4). Fig. S5 demonstrates that neutrophils transfer lipids to tumor cells to promote cell proliferation and AST (related to Figs. 5 and 6).

### Data availability

RNA-seq data of mouse tumors of the *KL* model used in this study are openly available in the National Omics Data Encyclopedia under accession no. OEP002019 (Fang et al., 2023).

## Acknowledgments

We thank Dr. T. Jacks (Massachusetts Institute of Technology, Cambridge, MA, USA) for providing $Kras^{LSL\text{-}G12D/+}$ mouse, Dr. Ronald DePinho (The University of Texas MD Anderson Cancer Center, Houston, TX, USA) for $Lkb1^{L/L}$ mouse, and Dr. Guoliang Xu (Center for Excellence in Molecular Cell Science, Shanghai, China) for $Tet2^{L/L}$ mouse and plasmids.

This work was supported by the National Key Research and Development Program of China (grants 2022YFA1103900 to H. Ji, 2020YFA0803300 to H. Ji); the National Natural Science Foundation of China (grants 82341002 to H. Ji, 82030083 to H. Ji, 32293192 to H. Ji, 31821002 to D. Ye, 31871431 to D. Ye, 82173340 to L. Hu, 32100593 to X. Tong, 82372763 to X. Wang, 82303039 to Z. Qin, and 82303575 to S. Tang); the Basic Frontier Scientific Research Program of Chinese Academy of Science (ZDBS-LY-SM006 to H. Ji); the Innovative Research Team of High-Level Local Universities in Shanghai (SSMU-ZLCX20180500 to H. Ji); the Science and Technology Commission of Shanghai Municipality (21ZR1470300 to L. Hu); and the Shanghai Sailing Program (23YF1452900 to Z. Qin).

Author contributions: Y. Xue: Conceptualization, Investigation, Validation, Writing—original draft, Writing—review and editing, Yuting Chen: Investigation, Validation, S. Sun: Investigation, Writing—review and editing, X. Tong: Resources, Yujia Chen: Formal analysis, Investigation, Validation, S. Tang: Formal analysis, X. Wang: Funding acquisition, Investigation, S. Bi: Validation, Y. Qiu: Resources, Q. Zhao: Validation, Z. Qin: Resources, Validation, Q. Xu: Investigation, Y. Ai: Validation, Leilei Chen: Resources, B. Zhang: Resources, Software, Writing—review and editing, Z. Liu: Software, M. Ji: Methodology, Supervision, M. Lang: Conceptualization, Investigation, Supervision, Luonan Chen: Data curation, Funding acquisition, Investigation, Methodology, Supervision, G. Xu: Conceptualization, Supervision, Writing—review and editing, L. Hu: Funding acquisition, Supervision, Writing—original draft, Writing—review and editing, D. Ye: Conceptualization, Project administration, Resources, Supervision, Writing—review and editing, H. Ji: Conceptualization, Funding acquisition, Project administration, Supervision, Writing—original draft, Writing—review and editing.

Disclosures: M. Lang reported non-financial support from the East China University of Science and Technology during the conduct of the study. No other disclosures were reported.

Submitted: 18 January 2024
Revised: 21 March 2024
Accepted: 5 April 2024

## References

Ab Mutalib, N.S., S.E. Syafruddin, R.R. Md Zain, A.Z. Mohd Dali, R.I. Mohd Yunos, S. Saidin, R. Jamal, and N.M. Mokhtar. 2014. Molecular characterization of serous ovarian carcinoma using a multigene next generation sequencing cancer panel approach. *BMC Res. Notes.* 7:805. https://doi.org/10.1186/1756-0500-7-805

Ajayi, S., H. Becker, H. Reinhardt, M. Engelhardt, R. Zeiser, N. von Bubnoff, and R. Wäsch. 2018. Ruxolitinib. *Recent Results Cancer Res.* 212:119–132. https://doi.org/10.1007/978-3-319-91439-8_6

Aran, D., M. Sirota, and A.J. Butte. 2015. Systematic pan-cancer analysis of tumour purity. *Nat. Commun.* 6:8971. https://doi.org/10.1038/ncomms9971

Awad, M.M., S. Liu, I.I. Rybkin, K.C. Arbour, J. Dilly, V.W. Zhu, M.L. Johnson, R.S. Heist, T. Patil, G.J. Riely, et al. 2021. Acquired resistance to KRAS$^{G12C}$ inhibition in cancer. *N. Engl. J. Med.* 384:2382–2393. https://doi.org/10.1056/NEJMoa2105281

Banks, K.M., Y. Lan, and T. Evans. 2021. Tet proteins regulate neutrophil granulation in zebrafish through demethylation of socs3b mRNA. *Cell Rep.* 34:108632. https://doi.org/10.1016/j.celrep.2020.108632

Bardeesy, N., M. Sinha, A.F. Hezel, S. Signoretti, N.A. Hathaway, N.E. Sharpless, M. Loda, D.R. Carrasco, and R.A. DePinho. 2002. Loss of the Lkb1 tumour suppressor provokes intestinal polyposis but resistance to transformation. *Nature.* 419:162–167. https://doi.org/10.1038/nature01045

Camolotto, S.A., S. Pattabiraman, T.L. Mosbruger, A. Jones, V.K. Belova, G. Orstad, M. Streiff, L. Salmond, C. Stubben, K.H. Kaestner, and E.L. Snyder. 2018. FoxA1 and FoxA2 drive gastric differentiation and suppress squamous identity in NKX2-1-negative lung cancer. *Elife.* 7:e38579. https://doi.org/10.7554/eLife.38579

Català-Moll, F., A.G. Ferreté-Bonastre, G. Godoy-Tena, O. Morante-Palacios, L. Ciudad, L. Barberà, F. Fondelli, E.M. Martínez-Cáceres, J. Rodríguez-Ubreva, T. Li, and E. Ballestar. 2022. Vitamin D receptor, STAT3, and TET2 cooperate to establish tolerogenesis. *Cell Rep.* 38:110244. https://doi.org/10.1016/j.celrep.2021.110244

Chen, L.L., H.P. Lin, W.J. Zhou, C.X. He, Z.Y. Zhang, Z.L. Cheng, J.B. Song, P. Liu, X.Y. Chen, Y.K. Xia, et al. 2018. SNIP1 recruits TET2 to regulate c-MYC target genes and cellular DNA damage response. *Cell Rep.* 25:1485–1500.e4. https://doi.org/10.1016/j.celrep.2018.10.028

Chen, L.L., C. Morcelle, Z.L. Cheng, X. Chen, Y. Xu, Y. Gao, J. Song, Z. Li, M.D. Smith, M. Shi, et al. 2022. Itaconate inhibits TET DNA dioxygenases to dampen inflammatory responses. *Nat. Cell Biol.* 24:353–363. https://doi.org/10.1038/s41556-022-00853-8

Chen, Y., Y. Xue, Y. Jin, and H. Ji. 2021. Lung stem cells in regeneration and tumorigenesis. *J. Genet. Genomics.* 48:268–276. https://doi.org/10.1016/j.jgg.2020.12.004

Cong, B., Q. Zhang, and X. Cao. 2021. The function and regulation of TET2 in innate immunity and inflammation. *Protein Cell.* 12:165–173. https://doi.org/10.1007/s13238-020-00796-6

Dai, H.Q., B.A. Wang, L. Yang, J.J. Chen, G.C. Zhu, M.L. Sun, H. Ge, R. Wang, D.L. Chapman, F. Tang, et al. 2016. TET-mediated DNA demethylation controls gastrulation by regulating Lefty-Nodal signalling. *Nature.* 538:528–532. https://doi.org/10.1038/nature20095

Dai, Y., S. Wang, W. Shi, and M. Lang. 2017. pH-responsive carboxymethyl chitosan-derived micelles as apatinib carriers for effective anti-angiogenesis activity: Preparation and in vitro evaluation. *Carbohydr. Polym.* 176:107–116. https://doi.org/10.1016/j.carbpol.2017.08.011

Delhommeau, F., S. Dupont, V. Della Valle, C. James, S. Trannoy, A. Massé, O. Kosmider, J.P. Le Couedic, F. Robert, A. Alberdi, et al. 2009. Mutation in TET2 in myeloid cancers. *N. Engl. J. Med.* 360:2289–2301. https://doi.org/10.1056/NEJMoa0810069

Detre, S., G. Saclani Jotti, and M. Dowsett. 1995. A "quickscore" method for immunohistochemical semiquantitation: Validation for oestrogen receptor in breast carcinomas. *J. Clin. Pathol.* 48:876–878. https://doi.org/10.1136/jcp.48.9.876

Dobin, A., C.A. Davis, F. Schlesinger, J. Drenkow, C. Zaleski, S. Jha, P. Batut, M. Chaisson, and T.R. Gingeras. 2013. STAR: Ultrafast universal RNA-seq aligner. *Bioinformatics.* 29:15–21. https://doi.org/10.1093/bioinformatics/bts635

Dumitru, C.A., S. Lang, and S. Brandau. 2013. Modulation of neutrophil granulocytes in the tumor microenvironment: Mechanisms and consequences for tumor progression. *Semin. Cancer Biol.* 23:141–148. https://doi.org/10.1016/j.semcancer.2013.02.005

DuPage, M., A.L. Dooley, and T. Jacks. 2009. Conditional mouse lung cancer models using adenoviral or lentiviral delivery of Cre recombinase. *Nat. Protoc.* 4:1064–1072. https://doi.org/10.1038/nprot.2009.95

Fang, Z., X. Han, Y. Chen, X. Tong, Y. Xue, S. Yao, S. Tang, Y. Pan, Y. Sun, X. Wang, et al. 2023. Oxidative stress-triggered Wnt signaling perturbation characterizes the tipping point of lung adeno-to-squamous transdifferentiation. *Signal Transduct. Target. Ther.* 8:16. https://doi.org/10.1038/s41392-022-01227-0

Ferone, G., J.Y. Song, K.D. Sutherland, R. Bhaskaran, K. Monkhorst, J.P. Lambooij, N. Proost, G. Gargiulo, and A. Berns. 2016. SOX2 is the determining oncogenic switch in promoting lung squamous cell carcinoma from different cells of origin. *Cancer Cell.* 30:519–532. https://doi.org/10.1016/j.ccell.2016.09.001

Gao, Y., W. Zhang, X. Han, F. Li, X. Wang, R. Wang, Z. Fang, X. Tong, S. Yao, F. Li, et al. 2014. YAP inhibits squamous transdifferentiation of Lkb1-deficient lung adenocarcinoma through ZEB2-dependent DNp63 repression. *Nat. Commun.* 5:4629. https://doi.org/10.1038/ncomms5629

Goncalves, A., B. Gontero, M. Nowicki, M. Margier, G. Masset, M.J. Amiot, and E. Reboul. 2015. Micellar lipid composition affects micelle interaction with class B scavenger receptor extracellular loops. *J. Lipid Res.* 56:1123–1133. https://doi.org/10.1194/jlr.M057612

Guo, C., R. Wan, Y. He, S.H. Lin, J. Cao, Y. Qiu, T. Zhang, Q. Zhao, Y. Niu, Y. Jin, et al. 2022. Therapeutic targeting of the mevalonate-geranylgeranyl diphosphate pathway with statins overcomes chemotherapy resistance in small cell lung cancer. *Nat. Cancer.* 3:614–628. https://doi.org/10.1038/s43018-022-00358-1

Hai, J., H. Zhang, J. Zhou, Z. Wu, T. Chen, E. Papadopoulos, C.M. Dowling, V. Pyon, Y. Pan, J.B. Liu, et al. 2020. Generation of genetically engineered mouse lung organoid models for squamous cell lung cancers allows for the study of combinatorial immunotherapy. *Clin. Cancer Res.* 26:3431–3442. https://doi.org/10.1158/1078-0432.CCR-19-1627

Han, X., F. Li, Z. Fang, Y. Gao, F. Li, R. Fang, S. Yao, Y. Sun, L. Li, W. Zhang, et al. 2014. Transdifferentiation of lung adenocarcinoma in mice with Lkb1 deficiency to squamous cell carcinoma. *Nat. Commun.* 5:3261. https://doi.org/10.1038/ncomms4261

Hanahan, D. 2022. Hallmarks of cancer: New dimensions. *Cancer Discov.* 12:31–46. https://doi.org/10.1158/2159-8290.CD-21-1059

Hänzelmann, S., R. Castelo, and J. Guinney. 2013. GSVA: Gene set variation analysis for microarray and RNA-seq data. *BMC Bioinformatics*. 14:7. https://doi.org/10.1186/1471-2105-14-7

He, R., Y. Xu, L. Zhang, S. Ma, X. Wang, D. Ye, and M. Ji. 2017. Dual-phase stimulated Raman scattering microscopy for real-time two-color imaging. *Optica*. 4:44–47. https://doi.org/10.1364/OPTICA.4.000044

He, Y.F., B.Z. Li, Z. Li, P. Liu, Y. Wang, Q. Tang, J. Ding, Y. Jia, Z. Chen, L. Li, et al. 2011. Tet-mediated formation of 5-carboxylcytosine and its excision by TDG in mammalian DNA. *Science*. 333:1303–1307. https://doi.org/10.1126/science.1210944

Hou, S., X. Han, and H. Ji. 2016. Squamous transition of lung adenocarcinoma and drug resistance. *Trends Cancer*. 2:463–466. https://doi.org/10.1016/j.trecan.2016.08.002

Hu, H., H. Gehart, B. Artegiani, C. Löpez-Iglesias, F. Dekkers, O. Basak, J. van Es, S.M. Chuva de Sousa Lopes, H. Begthel, J. Korving, et al. 2018. Long-term expansion of functional mouse and human hepatocytes as 3D organoids. *Cell*. 175:1591–1606.e19. https://doi.org/10.1016/j.cell.2018.11.013

Huynh, J., A. Chand, D. Gough, and M. Ernst. 2019. Therapeutically exploiting STAT3 activity in cancer - using tissue repair as a road map. *Nat. Rev. Cancer*. 19:82–96. https://doi.org/10.1038/s41568-018-0090-8

Ito, S., A.C. D'Alessio, O.V. Taranova, K. Hong, L.C. Sowers, and Y. Zhang. 2010. Role of Tet proteins in 5mC to 5hmC conversion, ES-cell self-renewal and inner cell mass specification. *Nature*. 466:1129–1133. https://doi.org/10.1038/nature09303

Ito, S., L. Shen, Q. Dai, S.C. Wu, L.B. Collins, J.A. Swenberg, C. He, and Y. Zhang. 2011. Tet proteins can convert 5-methylcytosine to 5-formylcytosine and 5-carboxylcytosine. *Science*. 333:1300–1303. https://doi.org/10.1126/science.1210597

Jackson, E.L., N. Willis, K. Mercer, R.T. Bronson, D. Crowley, R. Montoya, T. Jacks, and D.A. Tuveson. 2001. Analysis of lung tumor initiation and progression using conditional expression of oncogenic K-ras. *Genes Dev.* 15:3243–3248. https://doi.org/10.1101/gad.943001

Ji, H., M.R. Ramsey, D.N. Hayes, C. Fan, K. McNamara, P. Kozlowski, C. Torrice, M.C. Wu, T. Shimamura, S.A. Perera, et al. 2007. LKB1 modulates lung cancer differentiation and metastasis. *Nature*. 448:807–810. https://doi.org/10.1038/nature06030

Jin, Y., Q. Zhao, W. Zhu, Y. Feng, T. Xiao, P. Zhang, L. Jiang, Y. Hou, C. Guo, H. Huang, et al. 2022. Identification of TAZ as the essential molecular switch in orchestrating SCLC phenotypic transition and metastasis. *Natl. Sci. Rev.* 9:nwab232. https://doi.org/10.1093/nsr/nwab232

Johnson, D.E., R.A. O'Keefe, and J.R. Grandis. 2018. Targeting the IL-6/JAK/STAT3 signalling axis in cancer. *Nat. Rev. Clin. Oncol.* 15:234–248. https://doi.org/10.1038/nrclinonc.2018.8

Jung, K.H., W. Yoo, H.L. Stevenson, D. Deshpande, H. Shen, M. Gagea, S.Y. Yoo, J. Wang, T.K. Eckols, U. Bharadwaj, et al. 2017. Multifunctional effects of a small-molecule STAT3 inhibitor on NASH and hepatocellular carcinoma in mice. *Clin. Cancer Res.* 23:5537–5546. https://doi.org/10.1158/1078-0432.CCR-16-2253

Kanazawa, H., M. Ebina, N. Ino-Oka, M. Shimizukawa, T. Takahashi, S. Fujimura, T. Imai, and T. Nukiwa. 2000. Transition from squamous cell carcinoma to adenocarcinoma in adenosquamous carcinoma of the lung. *Am. J. Pathol.* 156:1289–1298. https://doi.org/10.1016/S0002-9440(10)64999-1

Kasembeli, M.M., U. Bharadwaj, P. Robinson, and D.J. Tweardy. 2018. Contribution of STAT3 to inflammatory and fibrotic diseases and prospects for its targeting for treatment. *Int. J. Mol. Sci.* 19:2299. https://doi.org/10.3390/ijms19082299

Kim, S.M., T.T. Nguyen, A. Ravi, P. Kubiniok, B.T. Finicle, V. Jayashankar, L. Malacrida, J. Hou, J. Robertson, D. Gao, et al. 2018. PTEN deficiency and AMPK activation promote nutrient scavenging and anabolism in prostate cancer cells. *Cancer Discov.* 8:866–883. https://doi.org/10.1158/2159-8290.CD-17-1215

Koivunen, J.P., J. Kim, J. Lee, A.M. Rogers, J.O. Park, X. Zhao, K. Naoki, I. Okamoto, K. Nakagawa, B.Y. Yeap, et al. 2008. Mutations in the LKB1 tumour suppressor are frequently detected in tumours from Caucasian but not Asian lung cancer patients. *Br. J. Cancer*. 99:245–252. https://doi.org/10.1038/sj.bjc.6604469

Koyama, S., E.A. Akbay, Y.Y. Li, A.R. Aref, F. Skoulidis, G.S. Herter-Sprie, K.A. Buczkowski, Y. Liu, M.M. Awad, W.L. Denning, et al. 2016. STK11/LKB1 deficiency promotes neutrophil recruitment and proinflammatory cytokine production to suppress T-cell activity in the lung tumor microenvironment. *Cancer Res.* 76:999–1008. https://doi.org/10.1158/0008-5472.CAN-15-1439

Krause, A., L. Roma, T. Lorber, J. Habicht, D. Lardinois, M.R. De Filippo, S.S. Prince, S. Piscuoglio, C. Ng, and L. Bubendorf. 2020. Deciphering the clonal relationship between glandular and squamous components in adenosquamous carcinoma of the lung using whole exome sequencing. *Lung Cancer*. 150:132–138. https://doi.org/10.1016/j.lungcan.2020.10.013

Lan, F., R.E. Collins, R. De Cegli, R. Alpatov, J.R. Horton, X. Shi, O. Gozani, X. Cheng, and Y. Shi. 2007. Recognition of unmethylated histone H3 lysine 4 links BHC80 to LSD1-mediated gene repression. *Nature*. 448:718–722. https://doi.org/10.1038/nature06034

Langemeijer, S.M., R.P. Kuiper, M. Berends, R. Knops, M.G. Aslanyan, M. Massop, E. Stevens-Linders, P. van Hoogen, A.G. van Kessel, R.A. Raymakers, et al. 2009. Acquired mutations in TET2 are common in myelodysplastic syndromes. *Nat. Genet.* 41:838–842. https://doi.org/10.1038/ng.391

Leek, J.T., W.E. Johnson, H.S. Parker, A.E. Jaffe, and J.D. Storey. 2012. The sva package for removing batch effects and other unwanted variation in high-throughput experiments. *Bioinformatics*. 28:882–883. https://doi.org/10.1093/bioinformatics/bts034

Li, F., X. Han, F. Li, R. Wang, H. Wang, Y. Gao, X. Wang, Z. Fang, W. Zhang, S. Yao, et al. 2015. LKB1 inactivation elicits a redox imbalance to modulate non-small cell lung cancer plasticity and therapeutic response. *Cancer Cell*. 27:698–711. https://doi.org/10.1016/j.ccell.2015.04.001

Li, P., M. Lu, J. Shi, Z. Gong, L. Hua, Q. Li, B. Lim, X.H. Zhang, X. Chen, S. Li, et al. 2020a. Lung mesenchymal cells elicit lipid storage in neutrophils that fuel breast cancer lung metastasis. *Nat. Immunol.* 21:1444–1455. https://doi.org/10.1038/s41590-020-0783-5

Li, X., M. Wang, T. Gong, X. Lei, T. Hu, M. Tian, F. Ding, F. Ma, H. Chen, and Z. Liu. 2020b. A S100A14-CCL2/CXCL5 signaling axis drives breast cancer metastasis. *Theranostics*. 10:5687–5703. https://doi.org/10.7150/thno.42087

Lian, C.G., Y. Xu, C. Ceol, F. Wu, A. Larson, K. Dresser, W. Xu, L. Tan, Y. Hu, Q. Zhan, et al. 2012. Loss of 5-hydroxymethylcytosine is an epigenetic hallmark of melanoma. *Cell*. 150:1135–1146. https://doi.org/10.1016/j.cell.2012.07.033

Lin, G., C. Li, P.S. Li, W.Z. Fang, H.P. Xu, Y.H. Gong, Z.F. Zhu, Y. Hu, W.H. Liang, Q. Chu, et al. 2020. Genomic origin and EGFR-TKI treatments of pulmonary adenosquamous carcinoma. *Ann. Oncol.* 31:517–524. https://doi.org/10.1016/j.annonc.2020.01.014

Liu, J., S.N. Cho, B. Akkanti, N. Jin, J. Mao, W. Long, T. Chen, Y. Zhang, X. Tang, I.I. Wistub, et al. 2015. ErbB2 pathway activation upon Smad4 loss promotes lung tumor growth and metastasis. *Cell Rep.* 10:1599–1613. https://doi.org/10.1016/j.celrep.2015.02.014

Liu, J., T. Wang, C.J. Creighton, S.P. Wu, M. Ray, K.S. Janardhan, C.J. Willson, S.N. Cho, P.D. Castro, M.M. Ittmann, et al. 2019. JNK$^{1/2}$ represses Lkb$^{1}$-deficiency-induced lung squamous cell carcinoma progression. *Nat. Commun.* 10:2148. https://doi.org/10.1038/s41467-019-09843-1

Lu, Z., Liu, R., Wang, Y., Jiao, M., Li, Z., Wang, Z., Huang, C., Shi, G., Ke, A., Wang, L., et al. 2022. TET2 inactivation restrains IL-10-producing regulatory B cells to enable anti-tumor immunity in hepatocellular carcinoma. *Hepatology*. 77:745–759. https://doi.org/10.1002/hep.32442

Lussana, F., M. Cattaneo, A. Rambaldi, and A. Squizzato. 2018. Ruxolitinib-associated infections: A systematic review and meta-analysis. *Am. J. Hematol.* 93:339–347. https://doi.org/10.1002/ajh.24976

Mahoney, C.L., B. Choudhury, H. Davies, S. Edkins, C. Greenman, G. Haaften, T. Mironenko, T. Santarius, C. Stevens, M.R. Stratton, and P.A. Futreal. 2009. LKB1/KRAS mutant lung cancers constitute a genetic subset of NSCLC with increased sensitivity to MAPK and mTOR signalling inhibition. *Br. J. Cancer*. 100:370–375. https://doi.org/10.1038/sj.bjc.6604886

Matsumoto, S., R. Iwakawa, K. Takahashi, T. Kohno, Y. Nakanishi, Y. Matsuno, K. Suzuki, M. Nakamoto, E. Shimizu, J.D. Minna, and J. Yokota. 2007. Prevalence and specificity of LKB1 genetic alterations in lung cancers. *Oncogene*. 26:5911–5918. https://doi.org/10.1038/sj.onc.1210418

Modi, B., M. Hernandez-Henderson, D. Yang, J. Klein, S. Dadwal, E. Kopp, K. Huelsman, S. Mokhtari, H. Ali, M.M.A. Malki, et al. 2019. Ruxolitinib as salvage therapy for chronic graft-versus-host disease. *Biol. Blood Marrow Transplant.* 25:265–269. https://doi.org/10.1016/j.bbmt.2018.09.003

Mollaoglu, G., A. Jones, S.J. Wait, A. Mukhopadhyay, S. Jeong, R. Arya, S.A. Camolotto, T.L. Mosbruger, C.J. Stubben, C.J. Conley, et al. 2018. The lineage-defining transcription factors SOX2 and NKX2-1 determine lung cancer cell fate and shape the tumor immune microenvironment. *Immunity*. 49:764–779.e9. https://doi.org/10.1016/j.immuni.2018.09.020

Mukhopadhyay, A., K.C. Berrett, U. Kc, P.M. Clair, S.M. Pop, S.R. Carr, B.L. Witt, and T.G. Oliver. 2014. Sox2 cooperates with Lkb1 loss in a mouse

model of squamous cell lung cancer. *Cell Rep.* 8:40–49. https://doi.org/10.1016/j.celrep.2014.05.036

Nielsen, T.S., N. Jessen, J.O. Jørgensen, N. Møller, and S. Lund. 2014. Dissecting adipose tissue lipolysis: Molecular regulation and implications for metabolic disease. *J. Mol. Endocrinol.* 52:R199–R222. https://doi.org/10.1530/JME-13-0277

Palomino, D.C., and L.C. Marti. 2015. Chemokines and immunity. *Einstein.* 13:469–473. https://doi.org/10.1590/S1679-45082015RB3438

Pan, L., X. Chen, F.V. Rassool, C. Li, and J. Lin. 2022. LLL12B, a novel small-molecule STAT3 inhibitor, induces apoptosis and suppresses cell migration and tumor growth in triple-negative breast cancer cells. *Biomedicines.* 10:2003. https://doi.org/10.3390/biomedicines10082003

Perera, S.A., D. Li, T. Shimamura, M.G. Raso, H. Ji, L. Chen, C.L. Borgman, S. Zaghlul, K.A. Brandstetter, S. Kubo, et al. 2009. HER2YVMA drives rapid development of adenosquamous lung tumors in mice that are sensitive to BIBW2992 and rapamycin combination therapy. *Proc. Natl. Acad. Sci. USA.* 106:474–479. https://doi.org/10.1073/pnas.0808930106

Qin, Z., M. Yue, S. Tang, F. Wu, H. Sun, Y. Li, Y. Zhang, H. Izumi, H. Huang, W. Wang, et al. 2024. EML4-ALK fusions drive lung adeno-to-squamous transition through JAK-STAT activation. *J. Exp. Med.* 221:e20232028. https://doi.org/10.1084/jem.20232028

Quintanal-Villalonga, A., H. Taniguchi, Y.A. Zhan, M.M. Hasan, S.S. Chavan, F. Meng, F. Uddin, V. Allaj, P. Manoj, N.S. Shah, et al. 2021a. Comprehensive molecular characterization of lung tumors implicates AKT and MYC signaling in adenocarcinoma to squamous cell transdifferentiation. *J. Hematol. Oncol.* 14:170. https://doi.org/10.1186/s13045-021-01186-z

Quintanal-Villalonga, A., H. Taniguchi, Y.A. Zhan, M.M. Hasan, S.S. Chavan, F. Meng, F. Uddin, P. Manoj, M.T.A. Donoghue, H.H. Won, et al. 2021b. Multiomic analysis of lung tumors defines pathways activated in neuroendocrine transformation. *Cancer Discov.* 11:3028–3047. https://doi.org/10.1158/2159-8290.CD-20-1863

Ruiz, E.J., M.E. Diefenbacher, J.K. Nelson, R. Sancho, F. Pucci, A. Chakraborty, P. Moreno, A. Annibaldi, G. Liccardi, V. Encheva, et al. 2019. LUBAC determines chemotherapy resistance in squamous cell lung cancer. *J. Exp. Med.* 216:450–465. https://doi.org/10.1084/jem.20180742

Sanchez-Cespedes, M., P. Parrella, M. Esteller, S. Nomoto, B. Trink, J.M. Engles, W.H. Westra, J.G. Herman, and D. Sidransky. 2002. Inactivation of LKB1/STK11 is a common event in adenocarcinomas of the lung. *Cancer Res.* 62:3659–3662.

Sánchez-Rivera, F.J., T. Papagiannakopoulos, R. Romero, T. Tammela, M.R. Bauer, A. Bhutkar, N.S. Joshi, L. Subbaraj, R.T. Bronson, W. Xue, and T. Jacks. 2014. Rapid modelling of cooperating genetic events in cancer through somatic genome editing. *Nature.* 516:428–431. https://doi.org/10.1038/nature13906

Schoenfeld, A.J., J.M. Chan, D. Kubota, H. Sato, H. Rizvi, Y. Daneshbod, J.C. Chang, P.K. Paik, M. Offin, M.E. Arcila, et al. 2020. Tumor analyses reveal squamous transformation and off-target alterations as early resistance mechanisms to first-line osimertinib in EGFR-mutant lung cancer. *Clin. Cancer Res.* 26:2654–2663. https://doi.org/10.1158/1078-0432.CCR-19-3563

Shi, L., C. Zheng, Y. Shen, Z. Chen, E.S. Silveira, L. Zhang, M. Wei, C. Liu, C. de Sena-Tomas, K. Targoff, and W. Min. 2018. Optical imaging of metabolic dynamics in animals. *Nat. Commun.* 9:2995. https://doi.org/10.1038/s41467-018-05401-3

Siersbæk, R., V. Scabia, S. Nagarajan, I. Chernukhin, E.K. Papachristou, R. Broome, S.J. Johnston, S.E.P. Joosten, A.R. Green, S. Kumar, et al. 2020. IL6/STAT3 signaling hijacks estrogen receptor α enhancers to drive breast cancer metastasis. *Cancer Cell.* 38:412–423.e9. https://doi.org/10.1016/j.ccell.2020.06.007

Somerville, T.D., G. Biffi, J. Daßler-Plenker, S.K. Hur, X.Y. He, K.E. Vance, K. Miyabayashi, Y. Xu, D. Maia-Silva, O. Klingbeil, et al. 2020. Squamous trans-differentiation of pancreatic cancer cells promotes stromal inflammation. *Elife.* 9:e53381. https://doi.org/10.7554/eLife.53381

Spiegelman, B.M., and J.S. Flier. 2001. Obesity and the regulation of energy balance. *Cell.* 104:531–543. https://doi.org/10.1016/S0092-8674(01)00240-9

Tahiliani, M., K.P. Koh, Y. Shen, W.A. Pastor, H. Bandukwala, Y. Brudno, S. Agarwal, L.M. Iyer, D.R. Liu, L. Aravind, and A. Rao. 2009. Conversion of 5-methylcytosine to 5-hydroxymethylcytosine in mammalian DNA by MLL partner TET1. *Science.* 324:930–935. https://doi.org/10.1126/science.1170116

Tang, S., Y. Xue, Z. Qin, Z. Fang, Y. Sun, C. Yuan, Y. Pan, Y. Zhao, X. Tong, J. Zhang, et al. 2023. Counteracting lineage-specific transcription factor network finely tunes lung adeno-to-squamous transdifferentiation through remodeling tumor immune microenvironment. *Natl. Sci. Rev.* 10:nwad028. https://doi.org/10.1093/nsr/nwad028

Tata, P.R., R.D. Chow, S.V. Saladi, A. Tata, A. Konkimalla, A. Bara, D. Montoro, L.P. Hariri, A.R. Shih, M. Mino-Kenudson, et al. 2018. Developmental history provides a roadmap for the emergence of tumor plasticity. *Dev. Cell.* 44:679–693.e5. https://doi.org/10.1016/j.devcel.2018.02.024

Tong, X., A.S. Patel, E. Kim, H. Li, Y. Chen, S. Li, S. Liu, J. Dilly, K.S. Kapner, N. Zhang, et al. 2024. Adeno-to-squamous transition drives resistance to KRAS inhibition in LKB1 mutant lung cancer. *Cancer Cell.* 42:413–428.e7. https://doi.org/10.1016/j.ccell.2024.01.012

Traber, K.E., K.L. Hilliard, E. Allen, G.A. Wasserman, K. Yamamoto, M.R. Jones, J.P. Mizgerd, and L.J. Quinton. 2015. Induction of STAT3-dependent CXCL5 expression and neutrophil recruitment by oncostatin-M during pneumonia. *Am. J. Respir. Cell Mol. Biol.* 53:479–488. https://doi.org/10.1165/rcmb.2014-0342OC

Vance, J.E. 2015. Phospholipid synthesis and transport in mammalian cells. *Traffic.* 16:1–18. https://doi.org/10.1111/tra.12230

Wang, D., and R.N. Dubois. 2010. Eicosanoids and cancer. *Nat. Rev. Cancer.* 10:181–193. https://doi.org/10.1038/nrc2809

Wang, X., Y. Wang, Z. Fang, H. Wang, J. Zhang, L. Zhang, H. Huang, Z. Jiang, Y. Jin, X. Han, et al. 2021. Targeting HSPA1A in ARID2-deficient lung adenocarcinoma. *Natl. Sci. Rev.* 8:nwab014. https://doi.org/10.1093/nsr/nwab014

Wang, Y., J. Zhang, S. Ren, D. Sun, H.Y. Huang, H. Wang, Y. Jin, F. Li, C. Zheng, L. Yang, et al. 2019. Branched-chain amino acid metabolic reprogramming orchestrates drug resistance to EGFR tyrosine kinase inhibitors. *Cell Rep.* 28:512–525.e6. https://doi.org/10.1016/j.celrep.2019.06.026

Wong, A.L.A., J.L. Hirpara, S. Pervaiz, J.Q. Eu, G. Sethi, and B.C. Goh. 2017. Do STAT3 inhibitors have potential in the future for cancer therapy? *Expert Opin. Investig. Drugs.* 26:883–887. https://doi.org/10.1080/13543784.2017.1351941

Wu, H., and Y. Zhang. 2014. Reversing DNA methylation: Mechanisms, genomics, and biological functions. *Cell.* 156:45–68. https://doi.org/10.1016/j.cell.2013.12.019

Wu, Q., Y. Tian, J. Zhang, X. Tong, H. Huang, S. Li, H. Zhao, Y. Tang, C. Yuan, K. Wang, et al. 2018. In vivo CRISPR screening unveils histone demethylase UTX as an important epigenetic regulator in lung tumorigenesis. *Proc. Natl. Acad. Sci. USA.* 115:E3978–E3986. https://doi.org/10.1073/pnas.1716589115

Xiao, Z., Q. Jiang, J. Willette-Brown, S. Xi, F. Zhu, S. Burkett, T. Back, N.Y. Song, M. Datla, Z. Sun, et al. 2013. The pivotal role of IKKα in the development of spontaneous lung squamous cell carcinomas. *Cancer Cell.* 23:527–540. https://doi.org/10.1016/j.ccr.2013.03.009

Xu, C., C.M. Fillmore, S. Koyama, H. Wu, Y. Zhao, Z. Chen, G.S. Herter-Sprie, E.A. Akbay, J.H. Tchaicha, A. Altabef, et al. 2014. Loss of Lkb1 and Pten leads to lung squamous cell carcinoma with elevated PD-L1 expression. *Cancer Cell.* 25:590–604. https://doi.org/10.1016/j.ccr.2014.03.033

Xu, Q., C. Wang, J.X. Zhou, Z.M. Xu, J. Gao, P. Sui, C.P. Walsh, H. Ji, and G.L. Xu. 2022. Loss of TET reprograms Wnt signaling through impaired demethylation to promote lung cancer development. *Proc. Natl. Acad. Sci. USA.* 119:e2107599119. https://doi.org/10.1073/pnas.2107599119

Yang, L., Q. Liu, X. Zhang, X. Liu, B. Zhou, J. Chen, D. Huang, J. Li, H. Li, F. Chen, et al. 2020. DNA of neutrophil extracellular traps promotes cancer metastasis via CCDC25. *Nature.* 583:133–138. https://doi.org/10.1038/s41586-020-2394-6

Yao, S., X. Han, X. Tong, F. Li, Z. Qin, H.-Y. Huang, and J. Hongbin. 2018. Lysyl oxidase inhibition drives the transdifferentiation from lung adenocarcinoma to squamous cell carcinoma in mice. *bioRxiv.* https://doi.org/10.1101/314393 Preprint posted June 10, 2018.

Yin, Y., E. Morgunova, A. Jolma, E. Kaasinen, B. Sahu, S. Khund-Sayeed, P.K. Das, T. Kivioja, K. Dave, F. Zhong, et al. 2017. Impact of cytosine methylation on DNA binding specificities of human transcription factors. *Science.* 356:eaaj2239. https://doi.org/10.1126/science.aaj2239

Zhang, H., C. Fillmore Brainson, S. Koyama, A.J. Redig, T. Chen, S. Li, M. Gupta, C. Garcia-de-Alba, M. Paschini, G.S. Herter-Sprie, et al. 2017. Lkb1 inactivation drives lung cancer lineage switching governed by Polycomb Repressive Complex 2. *Nat. Commun.* 8:14922. https://doi.org/10.1038/ncomms14922

Zhang, Q., K. Zhao, Q. Shen, Y. Han, Y. Gu, X. Li, D. Zhao, Y. Liu, C. Wang, X. Zhang, et al. 2015a. Tet2 is required to resolve inflammation by recruiting Hdac2 to specifically repress IL-6. *Nature.* 525:389–393. https://doi.org/10.1038/nature15252

Zhang, W., Y. Gao, F. Li, X. Tong, Y. Ren, X. Han, S. Yao, F. Long, Z. Yang, H. Fan, et al. 2015b. YAP promotes malignant progression of Lkb1-deficient

lung adenocarcinoma through downstream regulation of survivin. *Cancer Res.* 75:4450–4457. https://doi.org/10.1158/0008-5472.CAN-14-3396

Zhao, S.G., W.S. Chen, H. Li, A. Foye, M. Zhang, M. Sjöström, R. Aggarwal, D. Playdle, A. Liao, J.J. Alumkal, et al. 2020. The DNA methylation landscape of advanced prostate cancer. *Nat. Genet.* 52:778–789. https://doi.org/10.1038/s41588-020-0648-8

Zhao, Y., J. Wang, W.N. Liu, S.Y. Fong, T.W.H. Shuen, M. Liu, S. Harden, S.Y. Tan, J.Y. Cheng, W.W.S. Tan, et al. 2021. Analysis and validation of human targets and treatments using a hepatocellular carcinoma-immune humanized mouse model. *Hepatology*. 74:1395–1410. https://doi.org/10.1002/hep.31812

Zlotnik, A., and O. Yoshie. 2000. Chemokines: A new classification system and their role in immunity. *Immunity*. 12:121–127. https://doi.org/10.1016/S1074-7613(00)80165-X

Zuo, E., Y.J. Cai, K. Li, Y. Wei, B.A. Wang, Y. Sun, Z. Liu, J. Liu, X. Hu, W. Wei, et al. 2017. One-step generation of complete gene knockout mice and monkeys by CRISPR/Cas9-mediated gene editing with multiple sgRNAs. *Cell Res.* 27:933–945. https://doi.org/10.1038/cr.2017.81

## Supplemental material

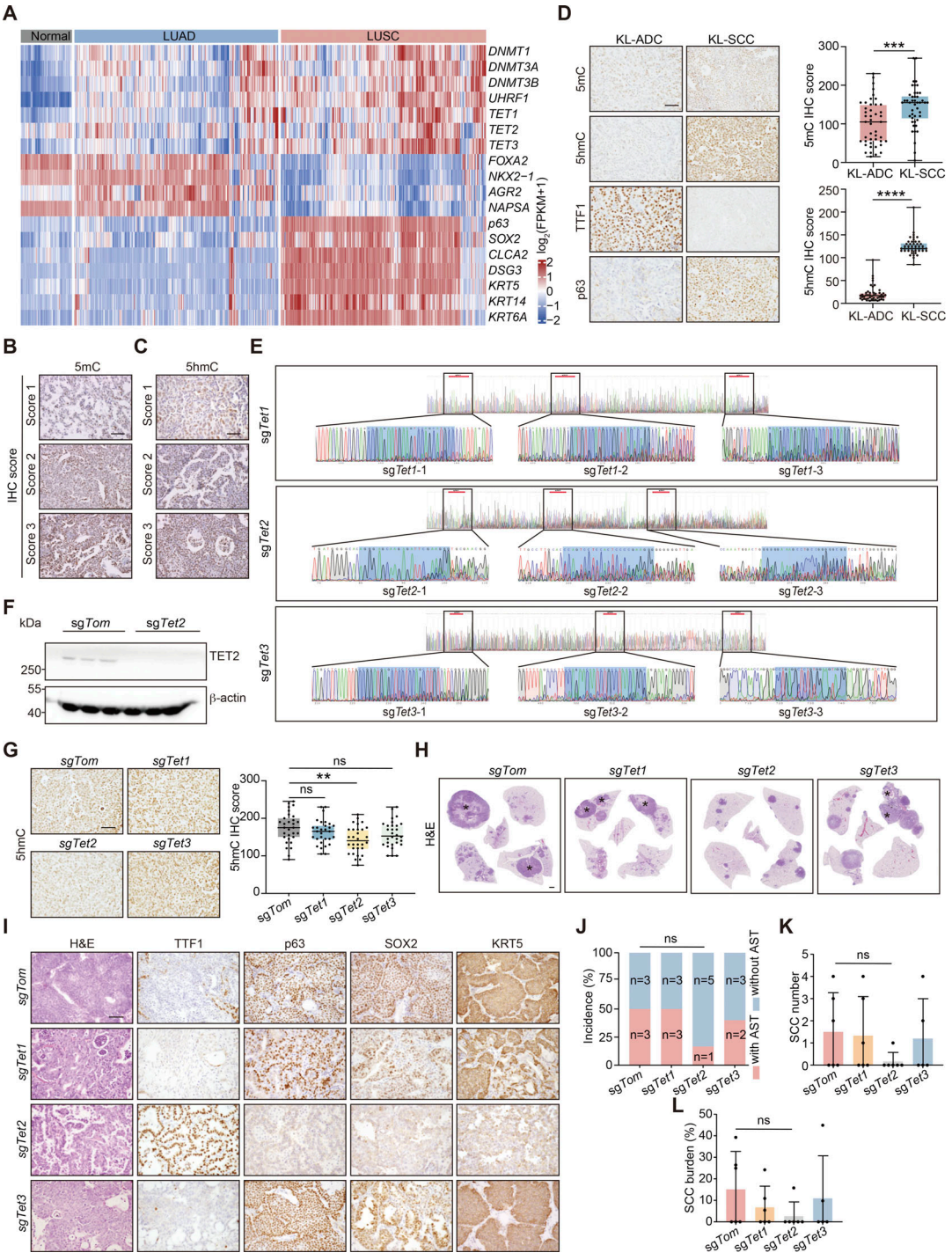


Figure S1. **CRISPR-mediated *Tet2* KO inhibits squamous transition in KL model. (A)** Heatmap of gene expression of DNA methylation regulators and lineage-defined biomarkers in human normal lung, LUAD, and LUSC (from TCGA dataset). **(B)** Representative IHC staining of various levels of 5mC (relative scores: 1, 2, 3). Scale bar: 50 µm. **(C)** Representative IHC staining of various intensity of 5hmC (relative scores: 1, 2, 3). Scale bar: 50 µm. **(D)** Representative IHC staining of 5mC, 5hmC, TTF1, and p63 in KL-ADC and KL-SCC. Scale bar: 50 µm. Statistical analyses are shown on the right. 45 representative images for each group were counted. **(E)** KO efficiency detection of sg*Tet1/2/3* through Sanger sequence. The targeting site is marked by box. **(F)** KO efficiency detection of sg*Tet2* through western blot in tumors with *Tet2* KO using lentivirus in *KL* mice. β-Actin served as the internal loading control. **(G)** Representative IHC staining of 5hmC in *KL* lung tumors with *Tet1/2/3* individual KOs. Scale bar: 50 µm. Statistical analyses are shown on the right. 30 representative images for each group were counted. **(H)** Representative H&E staining of whole mouse lungs with *Tet1/2/3* individual KOs. * indicates SCC. Scale bar: 1 mm. **(I)** Representative H&E and IHC staining for TTF1, p63, SOX2, and KRT5 in mouse lung tumors with *Tet1/2/3* individual KOs. Scale bar: 50 µm. **(J–L)** Statistical analyses of the AST incidence (J), the number (K), and burden (L) of SCC in *KL* mice with *Tet1/2/3* individual KOs (sg*Tom*: $n = 6$; sg*Tet1*: $n = 6$; sg*Tet2*: $n = 6$; sg*Tet3*: $n = 5$). Data in B–F represent one experiment of three independent repeats, and G–L represent one experiment of two independent repeats. **P < 0.01, ***P < 0.001, ****P < 0.0001 by two-tailed unpaired Student's *t* test (D), one-way ANOVA test (G, K and L), Fisher's exact test (J). ns: not significant. Data are represented as mean ± SD. Source data are available for this figure: SourceData FS1.

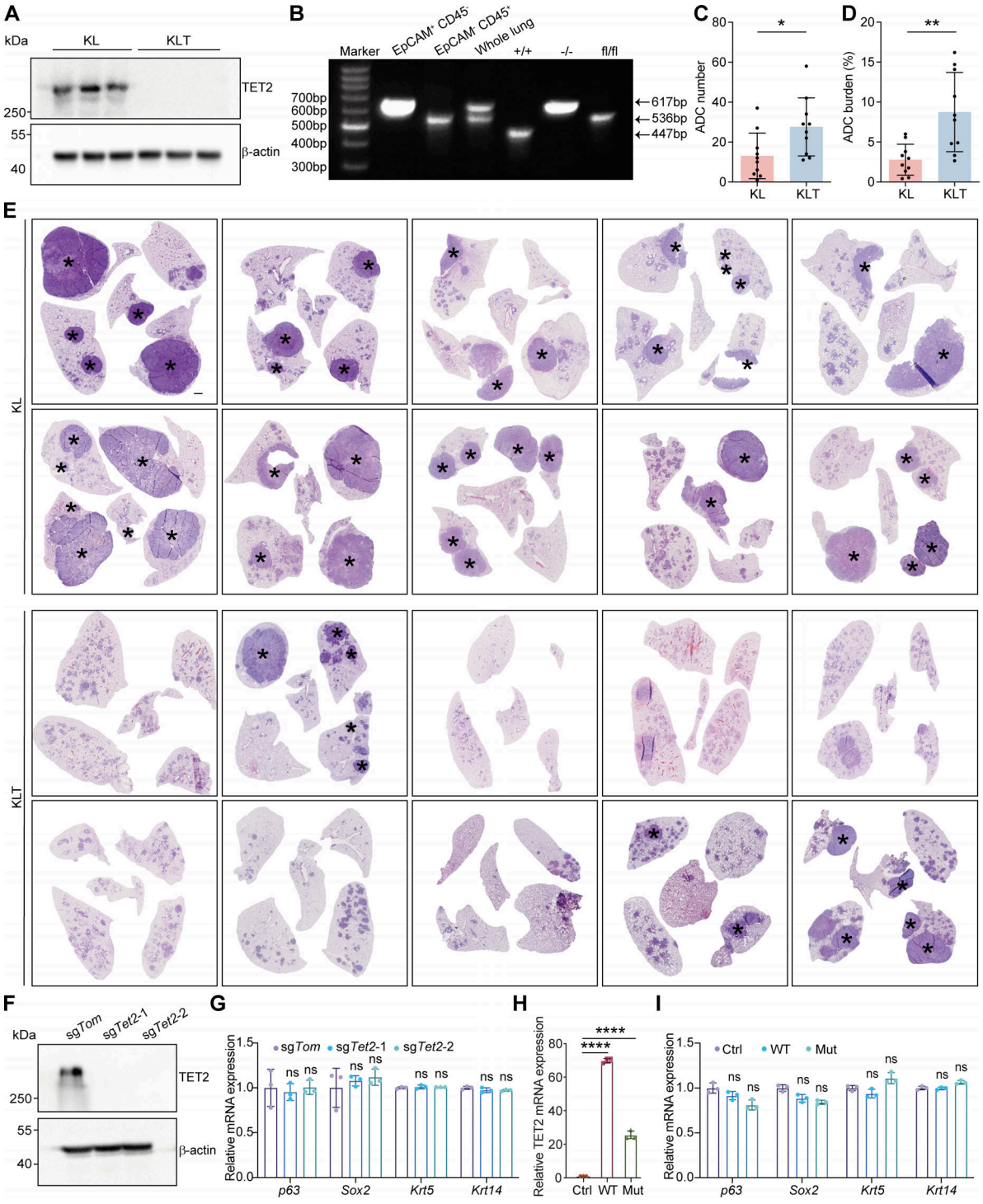


Figure S2. ***Tet2* KO inhibits lung AST in KL model. (A)** Western blot analysis for TET2 in *KL* and *KLT* tumors. β-Actin served as the internal loading control. **(B)** KO efficiency detection of *Tet2* in cancer cells (CD45⁻ EpCAM⁺), tumor-associated immune cells (CD45⁺ EpCAM⁻), and whole lung isolated from *KLT* tumors. "+/+" means the lung tissue isolated from wild-type mice. "−/−" means the homozygous deletion of *Tet2* gene alleles. "fl/fl" means the floxed *Tet2* gene alleles with intact gene expression before Cre administration. **(C and D)** Statistical analyses of number (C) and burden (D) of ADC in *KL* ($n$ = 10) and *KLT* ($n$ = 10) mice after 10 wk of Adeno-Cre treatment. **(E)** Representative H&E staining of whole lungs from *KL* and *KLT* mice. * indicates SCC. Scale bar: 1 mm. **(F)** Detection of TET2 protein in the *KL* squamous organoids with CRISPR-mediated *Tet2* KO by western blotting. β-Actin serves as an internal loading control. **(G)** Relative mRNA expression of *p63*, *Sox2*, *Krt5*, and *Krt14* in the *KL* squamous organoids upon *Tet2* KO by RT-qPCR. **(H)** Relative mRNA expression of TET2 in the *KL* squamous organoids after overexpressing wild-type (WT) and inactive mutant (Mut) TET2 by RT-qPCR. **(I)** Relative mRNA expression of *p63*, *Sox2*, *Krt5*, and *Krt14* in the *KL* squamous organoids after overexpressing wild-type (WT) and inactive mutant (Mut) TET2 by RT-qPCR. Data in A, B, and F–I represent one experiment of three independent repeats, and C–E represent one experiment of two independent repeats. *P < 0.05, **P < 0.01 by two-tailed unpaired Student's $t$ test (C and D), ****P < 0.0001 by one-way ANOVA test (G–I). ns: not significant. Data are represented as mean ± SD. Source data are available for this figure: SourceData FS2.

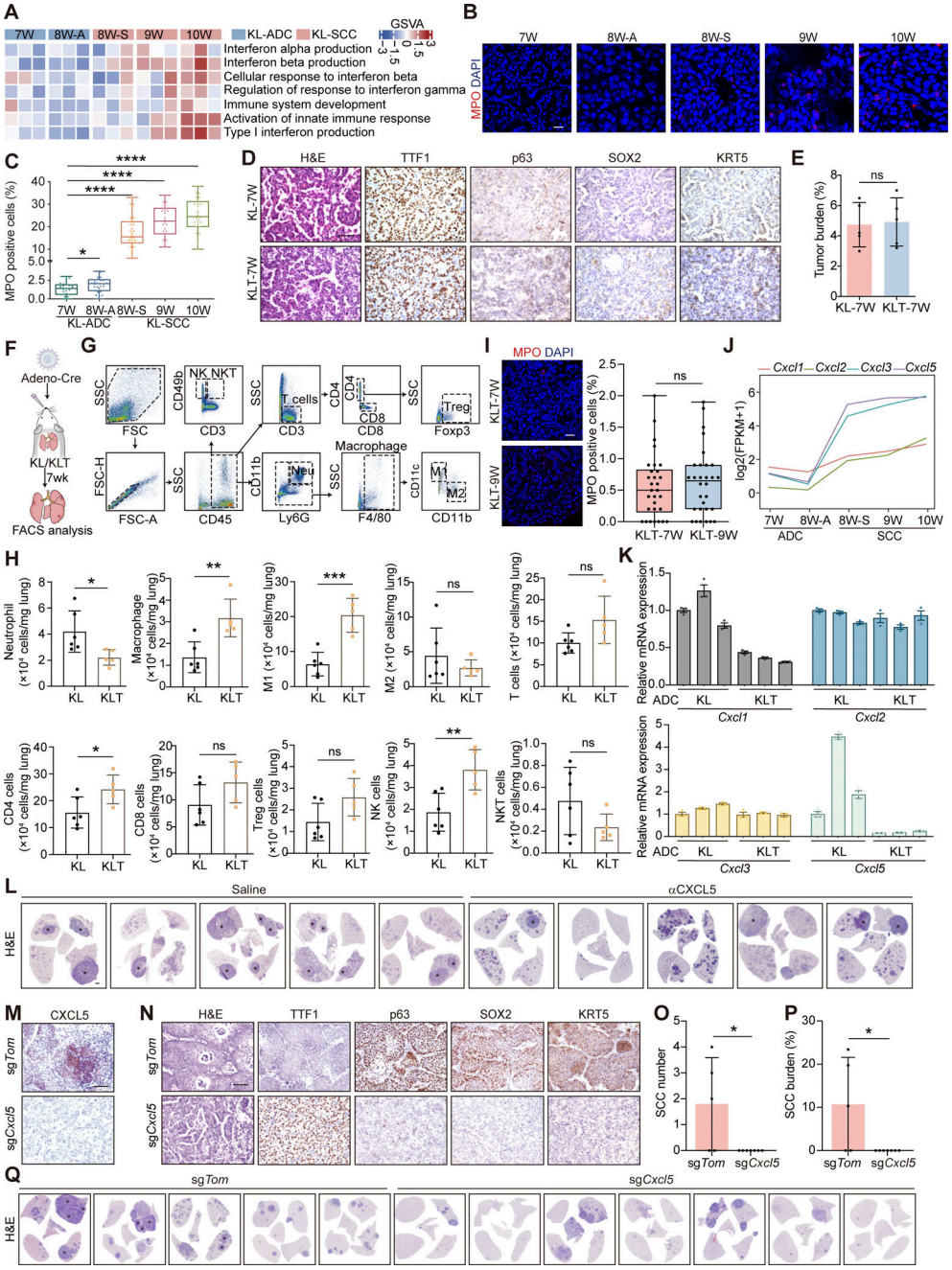

Figure S3. **TET2 promotes neutrophil infiltration potentially through the upregulation of CXCL5 expression. (A)** Heatmap of inflammatory and IFN signaling gene expression in *KL* tumors at serial time points. W, week. Both ADC and SCC were isolated from 8-wk time point, e.g., 8W-A means ADC and 8W-S means SCC. **(B)** Representative fluorescence staining of neutrophil (MPO-positive cells) infiltration in indicated *KL* tumors at serial time points. Neutrophil is indicated by MPO-positive cells. Red: MPO; blue: DAPI. Scale bar: 100 µm. **(C)** Statistical analyses of neutrophil (MPO-positive cells) infiltration in indicated *KL* tumors at a serial time points. 7W and 8W-A tumors analyzed were ADC and 8W-S, 9W, and 10W tumors analyzed were SCC. 30 representative images for each group were counted. **(D)** Representative H&E staining and IHC staining for TTF1, p63, SOX2, and KRT5 in lung tumors from *KL* or *KLT* mice after 7 wk (7W) of Adeno-Cre treatment. Scale bar: 50 µm. **(E)** Statistical analyses of tumor burden of *KL*-7W ($n$ = 5) and *KLT*-7W ($n$ = 5) mice. **(F)** Schematic illustration of immune infiltration analysis by FACS in *KL* and *KLT* mice. **(G)** Gating strategy for analyzing immune infiltration subtypes in *KL* and *KLT* mice. **(H)** The number of indicated immune subpopulations per mg lung were shown in *KL* ($n$ = 6) and *KLT* ($n$ = 5) models. Each dot represents one mouse. **(I)** Representative fluorescence staining of neutrophil (MPO-positive cells) infiltration in *KLT*-7W and *KLT*-9W tumors; red: MPO; blue: DAPI. Scale bar: 20 µm. Statistical analyses are shown on the right. **(J)** Relative expression of CXCL subfamily genes in *KL* tumors. **(K)** Relative mRNA expression of *Cxcl1*, *2*, *3*, and *5* in *KL* and *KLT* tumors by RT-qPCR. **(L)** Representative whole lungs of *KL* mice treated with saline and αCXCL5. * indicates SCC. Scale bar: 1 mm. **(M)** Representative IHC staining for CXCL5 in *KL* model with sg*Tom* or sg*Cxcl5*. Scale bar: 50 µm. **(N)** Representative H&E staining and IHC staining in *KL* model with sg*Tom* or sg*Cxcl5*. Scale bar: 50 µm. **(O and P)** Statistical analyses of the number (O) and burden (P) of SCC in *KL* model with sg*Tom* ($n$ = 5) or sg*Cxcl5* ($n$ = 7). **(Q)** Representative whole lungs of *KL* model with sg*Tom* or sg*Cxcl5*. * indicates SCC. Scale bar: 1 mm. Data in B, C, H, and K represent one experiment of three independent repeats, and D, E, I, and L–Q represent one experiment of two independent repeats. *P < 0.05, **P < 0.01, ***P < 0.001, ****P < 0.0001 by two-tailed unpaired Student's $t$ test (E, H, I, O, and P), one-way ANOVA test (C). ns: not significant. Data are represented as mean ± SD.

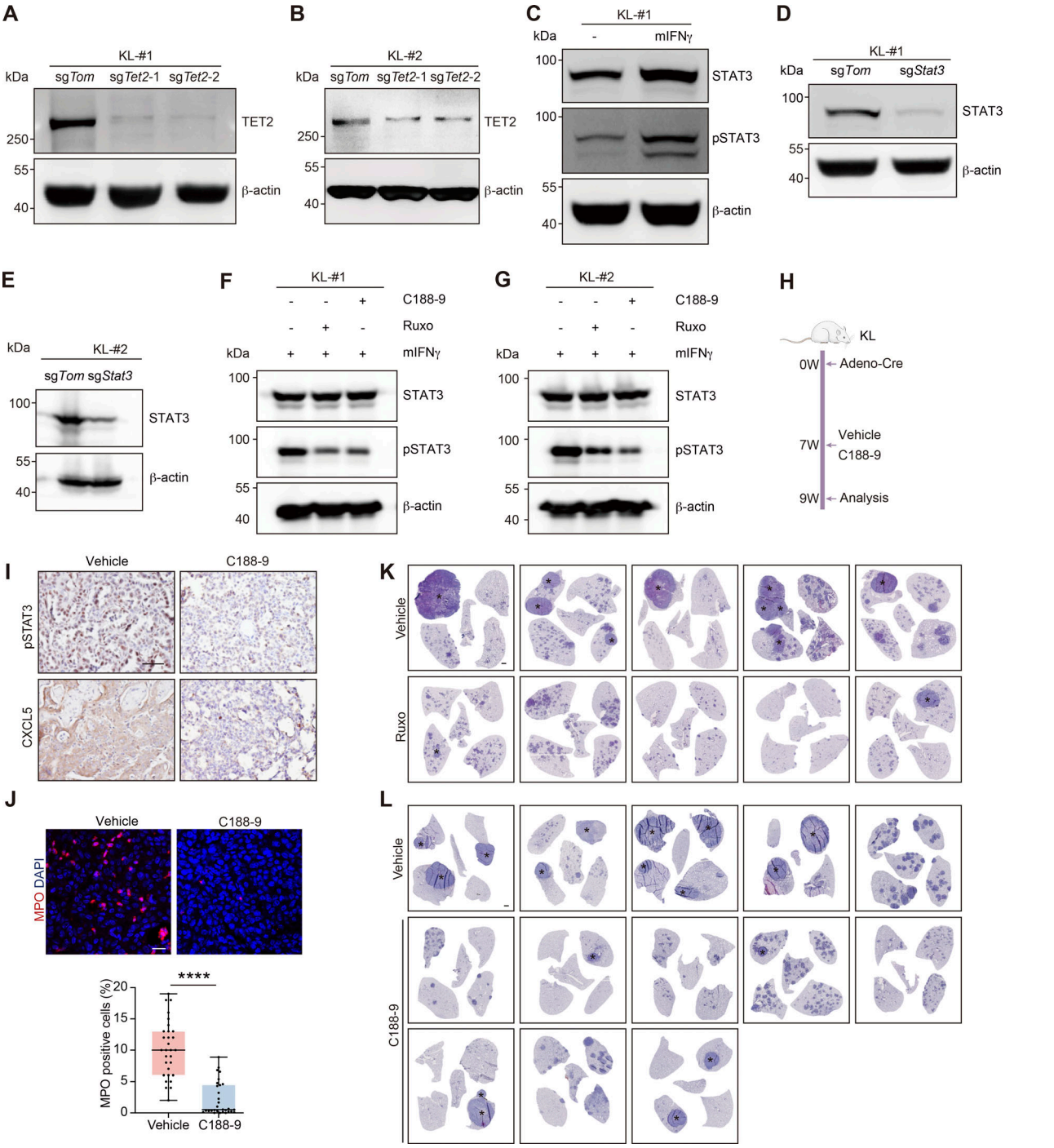


Figure S4. **TET2 interacts with STAT3 to transactivate *Cxcl5*. (A and B)** Western blot detection of TET2 in KL-#1 or KL-#2 cells with CRISPR-mediated *Tet2* KO. β-Actin served as the internal loading control. **(C)** Western blot detection of STAT3 and pSTAT3 in KL cells treated with 150 ng/ml mIFNγ for 24 h β-Actin served as the internal loading control. **(D and E)** Western blot analysis for STAT3 in KL-#1 or KL-#2 cells with CRISPR-mediated *Stat3* KO. β-Actin served as the internal loading control. **(F and G)** Western blot detection of STAT3 and pSTAT3 in KL cells treated with Ruxo (2 μM) and C188-9 (5 μM). β-Actin served as the internal loading control. **(H)** Schematic illustration of C188-9 treatment mouse experiment. W, week. **(I)** Representative IHC staining for pSTAT3 and CXCL5 in *KL* mice treated with vehicle and C188-9. Scale bar: 50 μm. **(J)** Representative fluorescence staining of neutrophil (MPO-positive cells) infiltration in *KL* tumors. red: MPO; blue: DAPI. Scale bar: 20 μm. The statistical fields include ADC and SCC pathologies. 30 representative images for each group were counted. **(K and L)** Representative whole lungs of *KL* mice treated with Ruxo (K) and C188-9 (L). * indicates SCC. Scale bar: 1 mm. Data in A–G represent one experiment of three independent repeats and I–L represent one experiment of two independent repeats. ****P < 0.0001 by two-tailed unpaired Student's *t* test (J). Data are represented as mean ± SD. Source data are available for this figure: SourceData FS4.

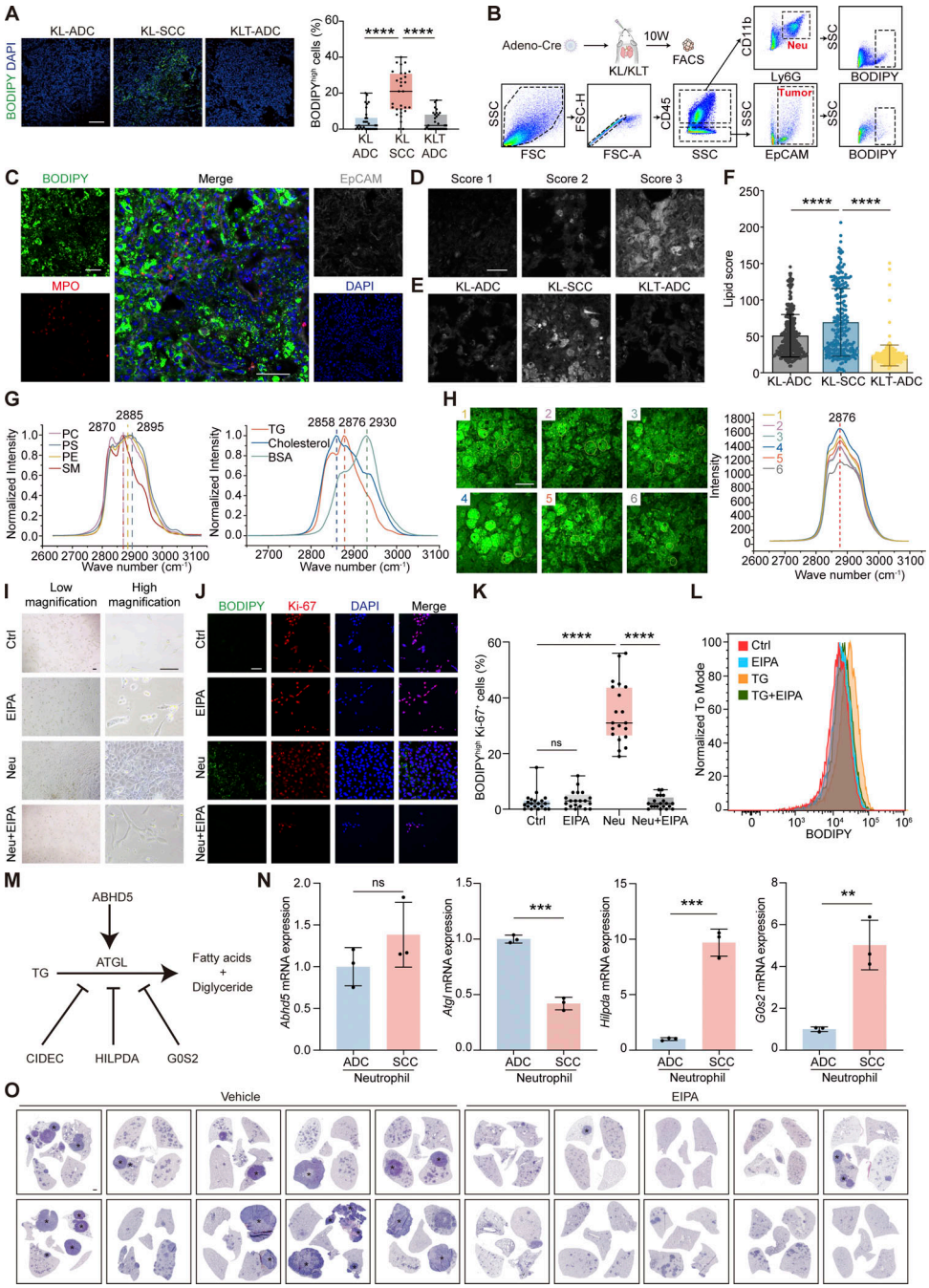


Figure S5. **Lipid-laden neutrophils transfer lipid to tumor cells to promote cell proliferation and AST. (A)** Representative fluorescence staining of KL-ADC, KL-SCC and KLT-ADC. green: lipid (BODIPY); blue: DAPI. Scale bar: 100 μm. Statistical analyses are shown on the right. 30 representative images for each group were counted. **(B)** Schematic illustration for lipid detection in neutrophil (Neu) and tumor cells isolated from *KL* and *KLT* tumors using FACS. W, week. **(C)** Representative fluorescence staining of KL-SCC; red: MPO; green: BODIPY; gray: EpCAM; blue: DAPI. Scale bar: 50 μm. **(D)** Representative SRS microscope images of various intensity of lipid (relative scores: 1, 2, 3). **(E and F)** (E) SRS microscope analysis for lipid level in KL-ADC, KL-SCC, and KLT-ADC. Lipid signal is indicated as gray. Statistical analyses are shown (F). 300 representative images for each group were counted. **(G)** The standard curves of TG, cholesterol, BSA, and phospholipids including PC, PS, PE, and SM were analyzed by SRS microscope. **(H)** Qualitative analysis of lipid in KL-SCC ($n$ = 6) by SRS microscope. The qualitative curves of lipid are shown on the right. Scale bar: 50 μm. **(I)** Cell morphology of KL-#2 cells monocultured (Ctrl) or cocultured with neutrophils (Neu) isolated from KL-SCC. EIPA was added to block lipid transport (Neu+EIPA). Scale bar: 100 μm. **(J and K)** (J) Representative fluorescence staining of BODIPY and Ki-67 in KL-#2 cells co-cultured with neutrophils. Scale bar: 100 μm. Statistical analyses were shown (K). 20 representative images for each group were counted. **(L)** KL cells were treated with TG-micelles (0.1 mM). EIPA was added to block TG transport. Lipid levels of KL cells were quantitated by FACS. **(M)** Diagram of the regulatory genes involved in TG hydrolysis. **(N)** Relative mRNA expression of *Abhd5*, *Atgl*, *Hilpda*, and *G0s2* in neutrophils isolated from KL-ADC and KL-SCC, which derived from 8W ADC and 8W SCC of *KL* model, respectively. *Cidec* has no signal. **(O)** Representative whole lungs of *KL* mice treated with vehicle or EIPA. * indicates SCC. Scale bar: 1 mm. Data in A, C–L, and N represent one experiment of three independent repeats and O represents one experiment of two independent repeats. **P < 0.01, ***P < 0.001, ****P < 0.0001 by one-way ANOVA test (A, F, and K), two-tailed unpaired Student's *t* test (*N*). ns: not significant. Data are represented as mean ± SD.